Monthly Notices of the ROYAL ASTRONOMICAL SOCIETY

MNRAS **514,** 4120–4139 (2022)
Advance Access publication 2022 May 30

https://doi.org/10.1093/mnras/stac1448

TESS discovery of a sub-Neptune orbiting a mid-M dwarf TOI-2136

Tianjun Gan [1]★ Abderahmane Soubkiou,[2,3,4] Sharon X. Wang,[1] Zouhair Benkhaldoun [2] Shude Mao,[1,5] Étienne Artigau,[6,7] Pascal Fouqué,[8,9] Luc Arnold,[8] Steven Giacalone,[10] Christopher A. Theissen,[11]† Christian Aganze,[11] Adam Burgasser,[11] Karen A. Collins [12] Avi Shporer,[13] Khalid Barkaoui [14,15,16] Mourad Ghachoui,[2,14] Steve B. Howell,[17] Claire Lamman,[12] Olivier D. S. Demangeon,[3,4] Artem Burdanov,[15] Charles Cadieux,[6] Jamila Chouqar,[2] Kevin I. Collins,[18] Neil J. Cook [6] Laetitia Delrez [14,19] Brice-Olivier Demory,[20] René Doyon,[6,7] Georgina Dransfield [21] Courtney D. Dressing,[10] Elsa Ducrot,[14,22] Jiahao Fan,[23] Lionel Garcia,[14] Holden Gill,[10] Michaël Gillon [14] Crystal L. Gnilka,[17,24] Yilen Gómez Maqueo Chew,[25] Maximilian N. Günther [26]‡ Christopher E. Henze,[17] Chelsea X. Huang,[13,27] Emmanuel Jehin,[19] Eric L. N. Jensen [28] Zitao Lin,[29] Nadine Manset,[8] James McCormac,[30] Catriona A. Murray [31] Prajwal Niraula,[15] Peter P. Pedersen,[31] Francisco J. Pozuelos,[14,19] Didier Queloz,[31,32] Benjamin V. Rackham [15]§ Arjun B. Savel,[33] Nicole Schanche [20] Richard P. Schwarz,[34] Daniel Sebastian,[21] Samantha Thompson,[31] Mathilde Timmermans,[14] Amaury H. M. J. Triaud [21] Michael Vezie,[13] Robert D. Wells,[20] Julien de Wit,[15] George R. Ricker,[13] Roland Vanderspek,[13] David W. Latham,[12] Sara Seager,[13,15,35] Joshua N. Winn[36] and Jon M. Jenkins[17]

Affiliations are listed at the end of the paper

Accepted 2022 May 20. Received 2022 April 27; in original form 2022 February 21

ABSTRACT

We present the discovery of TOI-2136 b, a sub-Neptune planet transiting a nearby M4.5V-type star every 7.85 d, identified through photometric measurements from the *Transiting Exoplanet Survey Satellite* (*TESS*) mission. The host star is located 33 pc away with a radius of $R_* = 0.34 \pm 0.02$ $R_\odot$, a mass of 0.34 ± 0.02 $M_\odot$, and an effective temperature of 3342 ± 100 K. We estimate its stellar rotation period to be 75 ± 5 d based on archival long-term photometry. We confirm and characterize the planet based on a series of ground-based multiwavelength photometry, high-angular-resolution imaging observations, and precise radial velocities from Canada–France–Hawaii Telescope (CFHT)/SpectroPolarimètre InfraROUge (SPIRou). Our joint analysis reveals that the planet has a radius of 2.20 ± 0.17 $R_\oplus$ and a mass of 6.4 ± 2.4 $M_\oplus$. The mass and radius of TOI-2136 b are consistent with a broad range of compositions, from water-ice to gas-dominated worlds. TOI-2136 b falls close to the radius valley for M dwarfs predicted by thermally driven atmospheric mass-loss models, making it an interesting target for future studies of its interior structure and atmospheric properties.

Key words: planets and satellites: detection – stars: individual: TIC 336128819 – TOI-2136 – planetary systems.

1 INTRODUCTION

The *Kepler* mission enabled the discovery of thousands of transiting exoplanets (Borucki et al. 2010), which began a new chapter in exoplanet research. One of the most important findings of *Kepler* is that super-Earths and sub-Neptunes ($1 < R_p < 4$ $R_\oplus$) are abundant in close-in orbits around other stars (Howard et al. 2012; Fressin et al. 2013; Petigura, Howard & Marcy 2013), whereas our Solar system has no such planets. Later demographic studies based on a well-characterized sample with refined stellar properties, as part of the California-*Kepler* Survey (CKS; Johnson et al. 2017; Petigura et al. 2017), revealed that the radius distribution of small planets has a bimodal profile with a valley centred at around 1.8 $R_\oplus$ (Fulton et al. 2017; Fulton & Petigura 2018). In particular, Van Eylen et al. (2018) and Martinez et al. (2019) looked into the radius distribution of small planets around stars with spectral types F, G, or K in a multidimensional parameter space. Both concluded that the location of the radius gap depends on the planet orbital period, and modelled it as a power-law function. This relation is consistent with the predictions from theoretical models of photoevaporation (Owen & Wu 2013, 2017; Jin et al. 2014; Lopez & Fortney 2014; Chen & Rogers 2016), which proposed that the H/He gaseous envelopes of small planets would be stripped away by high-energy stellar radiation such as X-rays during the first few Myr of the evolution when the

★ E-mail: gtj18@mails.tsinghua.edu.cn
† NASA Sagan Fellow.
‡ ESA Research Fellow.
§ 51 Pegasi b Fellow.

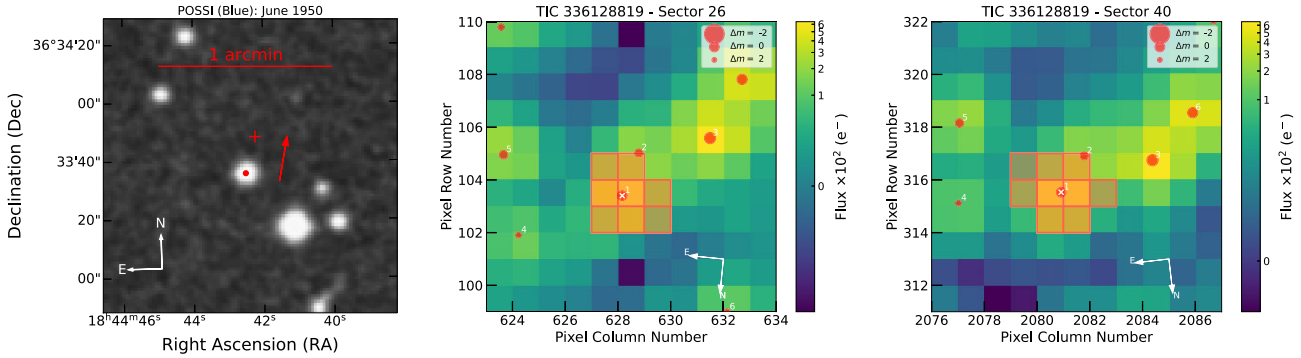

Figure 1. Left-hand panel: the POSSI blue image of TOI-2136 taken in 1950. The central red dot marks the position of TOI-2136 in this image, while the red cross represents its current location. Red arrow indicates the direction of proper motion. Middle and right-hand panels: TPFs of TOI-2136 in *TESS* Sectors 26 and 40, created with TPFPLOTTER. The orange shaded region represents the aperture used to extract the photometry. The red circles are the *Gaia* Data Release 2 (DR2) sources. Different sizes represent different magnitudes in contrast with TOI-2136.

host stars are still active (Lopez & Rice 2018). A similar trend arises according to the core-powered mass-loss theory (Ginzburg, Schlichting & Sari 2018; Lopez & Rice 2018; Gupta & Schlichting 2019, 2020, 2021). Under this hypothesis, the luminosity of cooling planetary cores offers the energy for atmosphere escape, and causes the planetary radius to shrink.

The transition radius between super-Earths and sub-Neptunes around M dwarfs tends to behave differently compared with Sun-like hosts. Cloutier & Menou (2020) investigated the radius valley of small planets around M dwarfs with a composite sample from *Kepler* and *K2* (Howell et al. 2014), and they found the slope of the valley likely follows a power-law relation with planet orbital period, but with an index of the opposite sign compared to the trend for Sun-like stars. Though this feature is in possible disagreement with the aforementioned thermally driven mass-loss models, it conforms to the gas-poor formation scenario (Lee, Chiang & Ormel 2014; Lee & Chiang 2016), implying that the radius gap is a result of the superposition of two distinct populations with the rocky group forming at late times when the protoplanetary disc had mostly dissipated. A straightforward way to pinpoint the dominant mechanism that results in the transition radius at the low stellar mass end is to examine the bulk compositions of small planets around M dwarfs (Cloutier & Menou 2020). Only a few (about 60) small planets around M dwarfs have been confirmed with both precise radius and mass determination so far (e.g. Charbonneau et al. 2009; Ment et al. 2019; Agol et al. 2021).

The *Transiting Exoplanet Survey Satellite* (*TESS*; Ricker et al. 2015) is performing an all-sky survey and targets bright nearby stars, providing an exciting opportunity to discover small transiting planets around M dwarfs. The *TESS* primary mission has already yielded the detections of several such systems (e.g. Vanderspek et al. 2019; Gan et al. 2020; Fukui et al. 2021; Wells et al. 2021). Some of those planets also have precise mass constraints through spectroscopic measurements since their hosts are relatively bright (e.g. Luque et al. 2019; Cloutier et al. 2020; Shporer et al. 2020; Soto et al. 2021). However, it is challenging to achieve a high enough signal-to-noise ratio (SNR) and obtain precise radial velocities (RVs) for mid-to-late M dwarfs as they are, in general, faint at optical wavelengths. The new-generation near-infrared (NIR) SpectroPolarimètre InfraROUge (SPIRou) spectrograph on the Canada–France–Hawaii Telescope (CFHT) opens a window to characterize planets around faint stars via high-precision velocimetry and spectropolarimetry (Donati et al. 2020; Klein et al. 2021; Gan et al. 2022).

Here we report the discovery and follow-up observations of a transiting sub-Neptune around the nearby M4.5V dwarf, TOI-2136. We present RV measurements from SPIRou along with a series of additional time series observations including ground-based photometry and high-resolution images that allow us to confirm that the *TESS* signal is due to a transiting planet. The rest of the paper is organized as follows. In Section 2, we detail all space- and ground-based observational data used in this work. Section 3 provides the stellar characterization. We present our analysis of light curves and the RVs in Section 4 before we discuss the properties and the prospects for future atmospheric characterization of TOI-2136 b in Section 5. A summary of our findings is given in Section 6.

2 OBSERVATIONS

2.1 *TESS* photometry

The *Transiting Exoplanet Survey Satellite* (*TESS*) observed TOI-2136 (TIC 336128819) on its Camera 1 with the 2-min cadence mode in Sector 26 from 2020 June 9 to 2020 July 4 and reobserved this target in Sector 40 between 2021 June 24 and 2021 July 23 during the extended mission. The left-hand panel of Fig. 1 shows the First Palomar Observatory Sky Survey (POSSI) image of TOI-2136 taken in 1950 (Abell 1955). Based on the relatively large stellar proper motion ($\sim$180 mas yr^{-1}), we rule out the possibility that light from an unassociated distant eclipsing binary system with $V \lesssim 21$ mag caused the *TESS* detection. The other panels of Fig. 1 show the target pixel files (TPFs) and the simple aperture photometry (SAP) apertures used in each sector, plotted with TPFPLOTTER(Aller et al. 2020). A nearby star (*Gaia* DR2 2096535788163295744, $T_{\rm mag} = 13.23$) 33 arcsec away is located at the edge of the *TESS* photometric aperture, and is expected to have a small light contamination. We take this into consideration in the joint fit (see Section 4.3). We summarize the host star properties in Table 1.

The raw *TESS* images were initially processed by the Science Processing Operations Center (SPOC; Jenkins et al. 2016) pipeline. The Presearch Data Conditioning (PDC; Smith et al. 2012; Stumpe et al. 2012, 2014) module was then applied to remove the instrumental systematic effects and generate a dilution-corrected light curve. Finally, a transit signal search was performed [Transiting Planet Search (TPS); Jenkins 2002; Jenkins et al. 2020], which leads to the detection of a 7.85-d periodic signal. Before the alert of this planet candidate, a suite of validation tests was carried out to rule out false

Table 1. Basic information of TOI-2136.

Parameter	Value	
Main identifiers		
TOI	2136	
TIC	336128819	
Gaia ID	2096535783864546944	
Equatorial coordinates		
RA (J2015.5)	18:44:42.32	
Dec. (J2015.5)	36:33:47.27	
Photometric properties		
TESS (mag)	11.737 ± 0.007	TIC V8[a]
Gaia (mag)	12.946 ± 0.011	*Gaia* EDR3[b]
Gaia BP (mag)	14.367 ± 0.010	*Gaia* EDR3
Gaia RP (mag)	11.780 ± 0.012	*Gaia* EDR3
J (mag)	10.184 ± 0.024	2MASS[c]
H (mag)	9.604 ± 0.028	2MASS
K (mag)	9.343 ± 0.022	2MASS
*WISE*1 (mag)	9.194 ± 0.022	*WISE*[d]
*WISE*2 (mag)	9.050 ± 0.021	*WISE*
*WISE*3 (mag)	8.924 ± 0.027	*WISE*
*WISE*4 (mag)	8.763 ± 0.328	*WISE*
Astrometric properties		
ϖ (mas)	29.976 ± 0.017	*Gaia* EDR3
μ_α (mas yr^{-1})	-33.81 ± 0.02	*Gaia* EDR3
μ_δ (mas yr^{-1})	177.05 ± 0.02	*Gaia* EDR3
RV (km s^{-1})	-28.8 ± 6.0	This work
Derived parameters		
Distance (pc)	33.36 ± 0.02	This work
$U_{\rm LSR}$ (km s^{-1})	-25.15 ± 2.26	This work
$V_{\rm LSR}$ (km s^{-1})	-9.42 ± 5.27	This work
$W_{\rm LSR}$ (km s^{-1})	13.16 ± 1.75	This work
M_* ($M_\odot$)	0.34 ± 0.02	This work
R_* ($R_\odot$)	0.34 ± 0.02	This work
ρ_* (g cm^{-3})	12.20 ± 2.53	This work
log g_* (cgs)	4.91 ± 0.03	This work
L_* ($L_\odot$)	0.013 ± 0.003	This work
$T_{\rm eff}$ (K)	3342 ± 100	This work
[Fe/H]	0.03 ± 0.07	This work
[M/H]	-0.01 ± 0.08	This work
$P_{\rm rot}$ (d)	75 ± 5	This work
Age (Gyr)	4.6 ± 1.0	This work

[a]Stassun et al. (2018, 2019); [b]Gaia Collaboration et al. (2021); [c]Cutri et al. (2003); [d]Wright et al. (2010).

positive scenarios and to perform an initial limb-darkened transit model fit (Twicken et al. 2018; Li et al. 2019).

We retrieved the Presearch Data Conditioning Simple Aperture Photometry (PDCSAP) light curve from the Mikulski Archive for Space Telescopes[1] (Twicken et al. 2010; Morris et al. 2020). We found a total of 16 941 and 15 319 measurements within the data from Sector 26 and Sector 40, respectively. In order to search for possible missing transit planets, we carried out an independent transit search using the transit least-squares (Hippke & Heller 2019) algorithm. We confirmed the 7.85 d signal with a signal detection efficiency of 34 but we did not find additional significant signals existing in the light curve. Generally, a signal with signal detection efficiency above 8 will be regarded as a significant detection. We thus treat this 7.85 d signal as a real transit event. To detrend the *TESS* light curve and remove the remaining systematic trends, we fit a Gaussian process (GP) model (Matérn-3/2 kernel) using the CELERITE package (Foreman-Mackey et al. 2017), after masking out all in-transit data. We show the SAP, raw PDCSAP, and detrended PDCSAP light curves in Fig. 2.

[1]http://archive.stsci.edu/tess/

2.2 Ground-based photometry

Because of the large pixel scale of *TESS* (21 arcsec pixel^{-1}; Ricker et al. 2015), the host star is likely blended with nearby stars in a single *TESS* pixel. Consequently, the transit signal of TOI-2136 detected in the *TESS* data could be caused by nearby eclipsing binaries. Even if the transit signal is on target, the depth might be biased to a smaller value because of light contamination. With all of the above in mind, we collected a series of ground-based observations of TOI-2136, as part of the *TESS* Follow-up Observing Program (TFOP),[2] to validate the planetary nature and refine both the transit ephemeris and the radius measurement. We scheduled these photometric time series by using the *TESS* Transit Finder (TTF) tool, which is a customized version of the TAPIR software package (Jensen 2013). We summarize the details in Table 2 and describe individual observations below. We show the raw and detrended ground-based light curves in Fig. 3 (see Section 4.1.2).

2.2.1 TRAPPIST-North

A total of three full transits of TOI-2136 b were acquired by the 60-cm robotic TRAnsiting Planets and PlanetesImals Small Telescope-North (TRAPPIST-North) on 2021 May 12, 2021 June 28, and 2021 July 6. TRAPPIST-North is located at Oukaimeden Observatory in Morocco (Gillon et al. 2011; Jehin et al. 2011; Barkaoui et al. 2019), which has an f/8 Ritchey–Chrétien optical design. It is equipped with a thermoelectrically cooled 2k × 2k Andor iKon-L BEX2-DD CCD camera with a pixel scale of 0.60 arcsec pixel^{-1}, resulting in a field of view of 20 × 20 arcmin^2. Because of the faintness of the host star, all of the three observations were carried out in the Sloan-z' filter with an exposure time of 20 s. We took a total of 441, 548, and 334 raw images during the three visits. Data calibration and photometric measurements were performed using a custom pipeline, PROSE,[3] which is detailed in Garcia et al. (2022). In all observations, the transit signal is detected on target.

2.2.2 LCOGT

We obtained two ground-based follow-up observations using the 1.0-m telescopes at Cerro Tololo Inter-American Observatory (CTIO), one of the Southern hemisphere sites of the Las Cumbres Observatory Global Telescope (LCOGT)[4] network (Brown et al. 2013). The photometric observations were acquired in the Panoramic Survey Telescope and Rapid Response System (Pan-STARRS) z-short band (z_s) with an exposure time of 80 s on 2021 June 21 and 2021 August 22, and both were done with the Sinistro cameras, which have a 26 × 26 arcmin^2 field of view and a plate scale of 0.389 arcsec pixel^{-1}. The images were focused and have stellar point spread functions (PSFs) with a full width at half-maximum (FWHM) of ∼2.0 and ∼3.1 arcsec, respectively. The raw images were first calibrated by the LCOGT standard automatic BANZAI pipeline (McCully et al. 2018). We then carried out photometric analysis using the ASTROIMAGEJ (AIJ) package (Collins et al. 2017) to extract the target light curve with

[2]https://tess.mit.edu/followup
[3]https://github.com/lgrcia/prose
[4]https://lco.global/

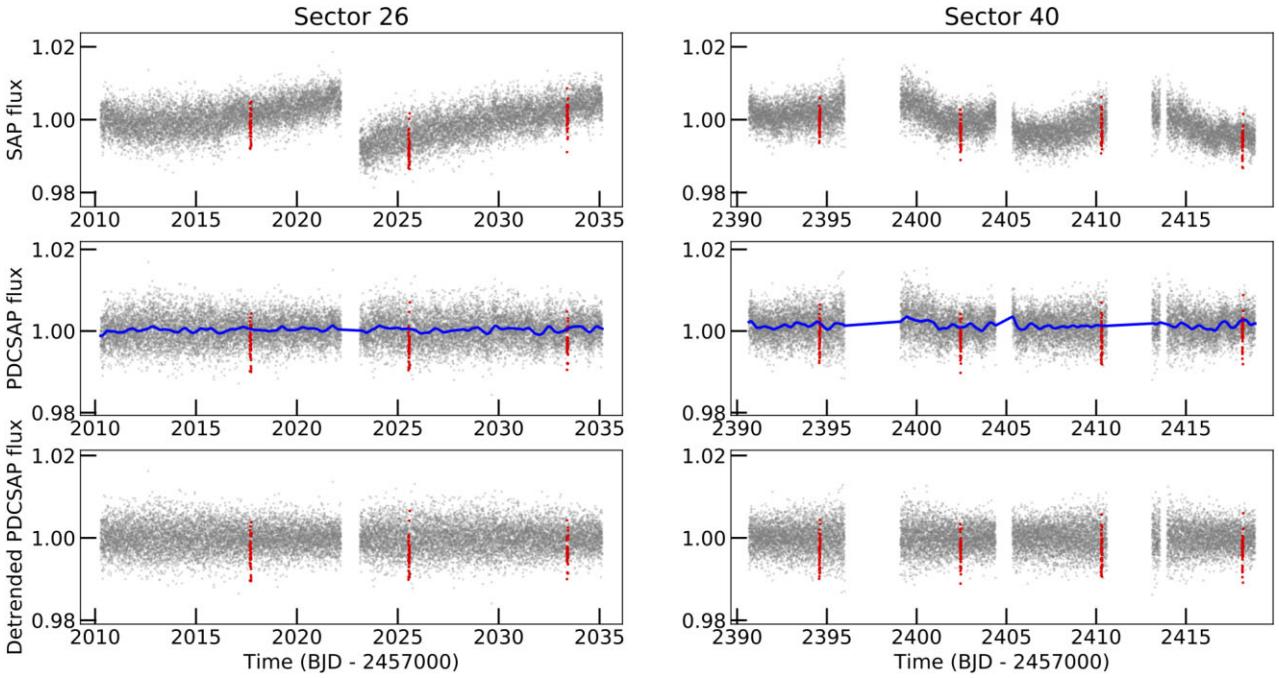

Figure 2. *TESS* light curves of TOI-2136 from Sectors 26 and 40. Top panels: the *TESS* SAP light curves. Middle panels: the *TESS* raw PDCSAP light curves after correcting the systematic and instrumental errors. The blue curves represent the best-fitting GP models used to remove the correlated noise existing in the PDCSAP light curves (Section 2.1). Bottom panels: the final detrended *TESS* PDCSAP light curves. The red dots highlight each transit of TOI-2136 b.

Table 2. Ground-based photometric follow-up observations for TOI-2136. The mid-wavelengths of z' and z_s are 966 and 870 nm, respectively.

Telescope	Pixel scale (arcsec)	Date (UT)	Filters	Aperture size (pixel)	PSF FWHM (arcsec)	No. of exposures	SNR[a]
Trappist-North-0.6 m	0.60	2021 May 12	z'	7.4	1.5	441	250
		2021 June 28	z'	9.2	1.5	548	330
		2021 July 6	z'	10.1	1.4	334	232
LCO-CTIO-1 m	0.39	2021 June 21	z_s	11.0	2.1	95	909
		2021 Aug 22	z_s	15.0	3.1	93	833
SPECULOOS-North-1 m	0.35	2021 Oct 24	z'	8.0	1.3	514	769

[a]We note that the values reported here are the signal-to-noise ratio (SNR) per point. The uncertainties of Las Cumbres Observatory (LCO) photometry might be underestimated.

uncontaminated apertures of 11 and 15 pixels (4.3 and 5.8 arcsec), and examine all nearby stars within 2.5 arcmin to look for the sources that may cause the *TESS* signal at the periods of the planet candidate (see Fig. 1). We confirmed the transit signal on target and ruled out the nearby eclipsing binary scenario.

2.2.3 *SPECULOOS-North*

We observed a full transit of TOI-2136 b with the 1.0-m SPECULOOS-North/Artemis telescope, located at Teide Observatory, Spain, on 2021 October 24. Artemis telescope is a Ritchey–Chrétien telescope equipped with a thermoelectrically cooled 2k × 2k Andor iKon-L BEX2-DD CCD camera with a pixel scale of 0.35 arcsec pixel^{-1} and a field of view of 12 × 12 arcmin^2. It is a twin of the four SPECULOOS-South telescopes located at the Paranal Observatory (Delrez et al. 2018; Sebastian et al. 2021), optimized for detecting planetary transits around cool stars (e.g. Niraula et al. 2020). The observations were done in the Sloan-z' filter in order to improve the transit SNR. The observation consisted of 514 raw images with an exposure time of 16 s, covering 137 min total. Data reduction and photometric measurements were performed using the PROSE pipeline (Garcia et al. 2022) with an uncontaminated aperture of 8 pixels (2.8 arcsec).

2.3 Spectroscopic observations

2.3.1 *IRTF/SpeX*

Infrared (IR) spectroscopy of TOI-2136 was obtained with the SpeX spectrograph (Rayner et al. 2003) on the 3.2-m NASA Infrared Telescope Facility (IRTF) on Maunakea, Hawaii, on 2021 September 15 (UT). Conditions were mostly clear with thin clouds and 0.7 arcsec seeing. The short-wavelength cross-dispersed (SXD) mode was used with the 0.5-arcsec-wide slit to obtain a 0.7–2.5 μm spectrum in seven orders at a spectral resolving power of ≈2000. A total of two ABBA nod sequences (eight exposures) were obtained with an integration time of 240 s per exposure with the slit aligned with the parallactic angle. The A0 V star HD 174567 ($V = 6.63$) was observed afterwards at an equivalent airmass for flux and telluric calibration, followed by arc lamp and flat-field lamp exposures. Data were reduced using SpeXtool v4.1 (Cushing, Vacca & Rayner 2004) using standard settings. The resulting spectrum of TOI-2136 had a median SNR of 200, with *JHK* peaks of around 250–300 (see Fig. 4).

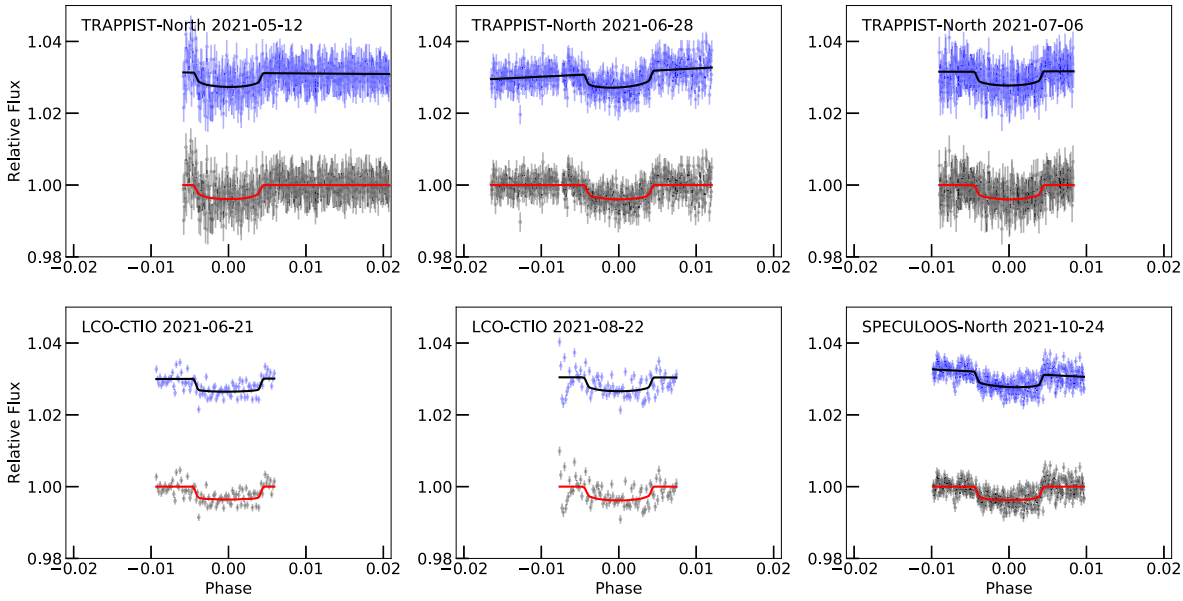

Figure 3. Ground-based light curves of TOI-2136. The blue dots are raw data. The black solid curve represents our best-fitting GP+transit model used to remove the systematic trends. The black dots are the final detrended light curves along with a best-fitting transit model, shown as a red solid curve (see Section 4.1.2). The facility and the observation date are listed at upper left in each panel.

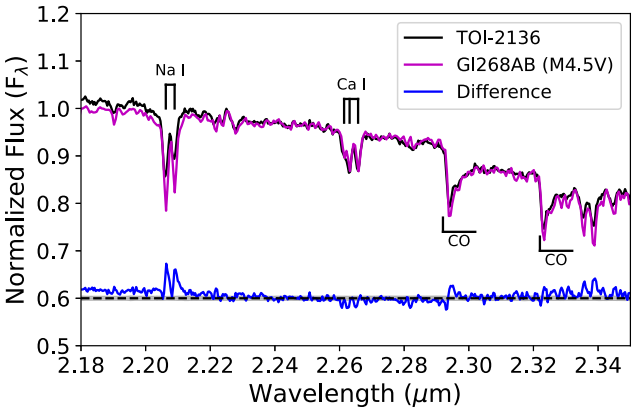

Figure 4. Normalized SpeX near-infrared (NIR) spectrum of TOI-2136 (black line) and the comparison spectrum (magenta line) taken from the IRTF library (Rayner, Cushing & Vacca 2009). Strong atomic and molecular features are marked. The difference between these two spectra is shown below (blue line). The NIR spectrum of TOI-2136 is consistent with a spectral type of M4.5V.

2.3.2 CFHT/SPIRou

TOI-2136 was monitored by SPIRou between 2021 April 24 and 2021 June 28. SPIRou has a spectral resolution of $R \approx 75\,000$, covering a bandwidth from 0.98 to 2.5 µm (Moutou et al. 2020). A total of 69 spectra were obtained. The observations were mainly conducted consecutively in two separate weeks, spanning roughly 50 d, with airmass below 1.3 and seeing at about 0.6 arcsec. We adopted an exposure time of 900 s, and we repeated the observations 2–4 times every night. The final spectra we obtained have a median SNR of 85 pixel^{-1} at Order 34 (*H* band). Since the *H*-band magnitude of TOI-2136 (9.6 mag) is brighter than the suggested limit 11 mag, we opted to use the Farby–Pérot (FP) mode to perform a simultaneous drift calibration during each observation, aiming for a RV precision better than 10 m s^{-1} (Cersullo et al. 2017).

The SPIRou data reduction was performed using the 0.7.194 version of the APERO pipeline (Cook et al., in preparation). Basic APERO steps have been described in a number of contributions (Artigau et al. 2021; Cristofari et al. 2022; Martioli et al. 2022). In brief, the major APERO modules are as follows.

(i) For all frames (science and calibrations), remove spatially correlated noise in the 4096 × 4096 images produced by the detector control software.
(ii) Locate orders in nightly calibrations.
(iii) Extract science and calibration frames into per order spectra.
(iv) Derive a nightly wavelength solution using the method described in Hobson et al. (2021).
(v) Measure the instantaneous drift in individual science frame relative to the nightly wavelength solution using the simultaneous FP measurements.
(vi) Apply a telluric correction to science data mainly based on a principal component analysis (PCA)-based approach (Artigau et al. 2014).
(vii) Using the line-by-line method (see below), and derive a RV.

Velocity measurements were obtained with the line-by-line (LBL) method (Artigau et al., submitted), which is discussed in Martioli et al. (2022). Overall the approach of the LBL is to subdivide the spectral domain in a large number of 'lines', typically 16 000 for SPIRou, that corresponds to domain between consecutive local maxima in spectrum. Within each line, one applies the Bouchy, Pepe & Queloz (2001) framework to the difference between a high SNR template and the spectrum to derive a velocity by projecting the residuals on to the first derivative of the template. The template is constructed from all observations of the target that are median-combined after registration to a common line-of-sight velocity, accounting for barycentric Earth motion. As SPIRou has slight large-scale chromatic transmission changes between visits due to effects such as changes in the seeing and injection efficiency, the large-scale structures of the input spectra are matched prior to median combination. This method provides a per line velocity and the corresponding uncertainty. One

then constructs a mixture model, where the mean velocity is derived simultaneously with the likelihood that a given line is valid (i.e. consistent with the mean velocity considering uncertainties) or that it belongs to a population of 'outliers' that should be disregarded. The LBL framework fully utilizes the RV content of the spectrum and significantly outperforms the cross-correlation function (CCF) in the NIR where numerous residuals (e.g. sky emission, telluric absorption, and detector defects) plague precise RV observations. One limit of the LBL framework is that it gives a very accurate relative velocity compared to a template, but does not directly provide an absolute velocity. To obtain an absolute velocity for our templates, we cross-correlate the mask obtained in defining 'lines' against a spectral model at the temperature of the star to derive a CCF. We use PHOENIX models (Husser et al. 2013) at $\log g = 5.0$ and the resulting CCF has a centre that is the negative of the systemic velocity of the star considered (-29.1 km s^{-1}). This systemic velocity is added on to the template-to-spectrum velocity measured.

All RVs we extracted are listed in Table A1. We dropped three outliers above the 3σ limit, and a total of 66 measurements were used in the following analysis.

2.4 High angular resolution imaging

High-resolution imaging is one of the standard follow-up observations made for exoplanet host stars. Spatially close companions, bound or close to the line of sight, can create a false-positive transit signal and provide 'third-light' flux leading to an underestimated planetary radius (Ciardi et al. 2015), incorrect planet and star properties (Furlan & Howell 2017, 2020), and may miss small planets in some exoplanetary systems (Lester et al. 2021). Additionally, close companions might play a role in the formation and evolution of planetary systems (Howell et al. 2021). Generally, *Gaia* is not capable to recover binaries with separations smaller than 0.7 arcsec (Ziegler et al. 2020). Therefore, we took high angular resolution imaging observations of TOI-2136 to search for its stellar companions beyond the detection limit of *Gaia*.

2.4.1 Robo-AO

As part of an M dwarf multiplicity survey (Lamman et al. 2020), sub-arcsecond imaging of TOI-2136 was previously obtained from Robo-AO, an autonomous laser-guided adaptive optics system (Baranec et al. 2014), on 2016 July 29 on the Kitt Peak 2.1-m telescope. The observation was taken with an Andor iXon DU-888 camera in the i'-band with a 90 s exposure time. Median seeing at the telescope was 1.44 arcsec that resulted in an i'-band Strehl ratio of 4.2 per cent for this observation and a FWHM of around 0.12 arcsec. The image was processed via an automatic pipeline, which shifts and adds data to optimize for both high and low SNR images (Jensen-Clem et al. 2018). Lamman et al. (2020) identified that there is no stellar companion of TOI-2136 with a contrast above the curve shown in Fig. 5.

2.4.2 Shane

We observed TOI-2136 on 2021 April 30 (UT) using the Shane Adaptive optics infraRed Camera-Spectrograph (ShARCS) camera on the Shane 3-m telescope at Lick Observatory (Kupke et al. 2012; Gavel et al. 2014; McGurk et al. 2014). Observations were taken with the Shane adaptive optics system in natural guide star mode. We refer the readers to Savel et al. (2020) for a detailed description of the observing strategy and reduction procedure. We collected two sequences of observations, one with a K_s filter ($\lambda_0 = 2.150$ µm, $\Delta\lambda = 0.320$ µm) and one with a J filter ($\lambda_0 = 1.238$ µm, $\Delta\lambda = 0.271$ µm). Our contrast curves are shown in Fig. 5. We find no nearby stellar companions within our detection limits.

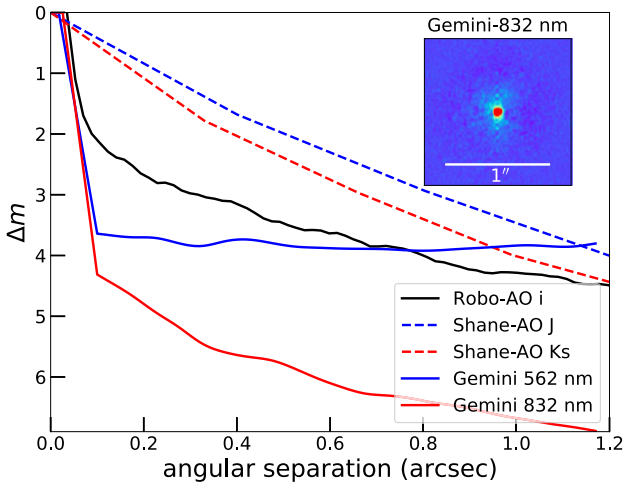

Figure 5. 5σ contrast curves for TOI-2136 from independent observations. The inset figure shows the reconstructed Gemini 832 nm image. TOI-2136 was found to be an isolated single star within the detection limits.

2.4.3 Gemini-North

We took a speckle imaging observation of TOI-2136 on 2021 October 17 (UT) using the 'Alopeke speckle instrument on the Gemini-North 8-m telescope (Scott et al. 2021). 'Alopeke provides simultaneous speckle imaging in two bands (562 and 832 nm) with output data products including a reconstructed image with robust contrast limits on companion detections (e.g. Howell et al. 2016). Five sets of 1000×0.06 s exposures were collected and subjected to Fourier analysis (see Howell et al. 2011 for details). We show the contrast curves of both 562 and 832 nm images and a reconstructed speckle image in Fig. 5. We find a result consistent with the above findings that TOI-2136 is isolated, with no companion brighter than 4–7 mag out to 1.2 arcsec, which corresponds to spatial limits of 0.7–40 au.

3 STELLAR PROPERTIES

3.1 Stellar characterization

The Two Micron All-Sky Survey (2MASS) K_s magnitude and the parallax from *Gaia* Early Data Release 3 (EDR3; Gaia Collaboration et al. 2021) yield $M_K = 6.73 \pm 0.02$ mag. Using the empirical relation reported by Mann et al. (2015), we obtain a stellar radius of $R_* = 0.34 \pm 0.01$ R$_\odot$, assuming a typical 3 per cent uncertainty. This is consistent with the estimation $R_* = 0.34 \pm 0.02$ R$_\odot$ within 1σ using the angular diameter relation in Boyajian, van Belle & von Braun (2014). Based on the polynomial relation between bolometric correction BC$_K$ and stellar colour $V - J$ found by Mann et al. (2015), we obtain a BC$_K$ of 2.73 ± 0.21 mag, leading to a bolometric magnitude $M_{\rm bol} = 9.46 \pm 0.22$ mag and a bolometric luminosity $L_* = 0.013 \pm 0.003$ L$_\odot$. We estimated the stellar effective temperature of TOI-2136 using two different methods. Combining the stellar radius and bolometric luminosity with the Stefan–Boltzmann law, we find $T_{\rm eff} = 3324 \pm 55$ K. Additionally, we also obtain $T_{\rm eff}$ following the empirical relation with stellar colour $V - J$ and $J - H$ reported by

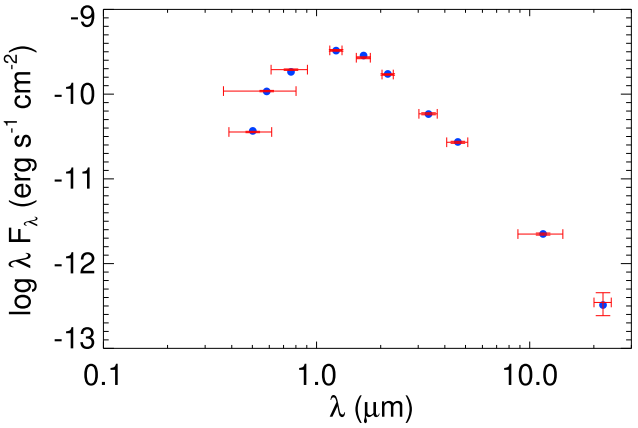

Figure 6. SED model for TOI-2136. The red symbols are the broad-band photometric measurements used in the SED analysis (provided in Table 1) with the horizontal uncertainty bars representing the effective width of the passband. The blue symbols are the model fluxes from the best-fitting Kurucz atmosphere model.

Mann et al. (2015) to find $T_{\rm eff} = 3314 \pm 104$ K. We evaluate the mass of TOI-2136 to be $M_* = 0.33 \pm 0.02$ M$_\odot$ using equation (2) in Mann et al. (2019). This estimation agrees with the value $M_* = 0.35 \pm 0.02$ M$_\odot$ given by the M_*–M_K empirical relation of Benedict et al. (2016).

We then performed an analysis of the broad-band spectral energy distribution (SED) of TOI-2136 using MIST stellar models (Choi et al. 2016; Dotter 2016) along with the *Gaia* EDR3 parallax (Gaia Collaboration et al. 2021) in order to derive the stellar parameters of TOI-2136. We make use of the EXOFASTV2 package (Eastman et al. 2019) to conduct the SED fit. We use the MIST method (the favoured method reported in Eastman et al. 2019, MISTSEDFILE) that interpolates the 4D grid of log g, $T_{\rm eff}$, [Fe/H], and an extinction grid from Conroy et al. (in preparation) to determine the bolometric corrections in each of the observed band. We include the $JHK_{\rm S}$ magnitudes from 2MASS (Cutri et al. 2003), the W1–W4 magnitudes from the *Wide-field Infrared Survey Explorer* (*WISE*; Wright et al. 2010), and three *Gaia* magnitudes G, $G_{\rm BP}$, $G_{\rm RP}$ (Gaia Collaboration et al. 2018) in the analysis. The available photometry spans a wavelength range from 0.5 to 22 μm (see Fig. 6). We set an upper limit on the V-band extinction from the dust maps of Schlafly & Finkbeiner (2011) and a Gaussian prior on the metallicity taken from the SpeX spectroscopic analysis. The EXOFASTV2 analysis ran until convergence when the Gelman–Rubin (GR) statistic and the number of independent chain draws (T_z) were less than 1.01 and greater than 1000, respectively. The full results of the SED fit are provided in Table 3, which are in excellent agreement with our previous estimation. Taking all the results above into account, we adopt the weighted-mean values of $T_{\rm eff}$, R_*, and M_* with conservative uncertainties and list all of them in Table 1. Combining the derived stellar radius with mass, we find a mean stellar density of $\rho_* = 12.2 \pm 2.5$ g cm^{-3}.

Finally, we also estimate the systemic RV of TOI-2136 to be -28.8 ± 6.0 km s^{-1} by RV correcting our SpeX spectrum using TELLRV (Newton et al. 2014). To determine the stellar type, we further compare our SpeX spectrum with the IRTF library (Rayner et al. 2009) and find that TOI-2136 is consistent with a star of spectral type M4.5V (Fig. 4). Lastly, we obtain the metallicity of TOI-2136 based on the relations defined in Mann et al. (2013) for cool dwarfs with spectral types between K5 and M5. Our analysis yields metallicities of [Fe/H] $= 0.03 \pm 0.07$ and [M/H] $= -0.01 \pm 0.08$, which are consistent with the SED result within 1σ.

Table 3. Median values and 68 per cent confidence interval for TOI-2136 from the spectral energy distribution (SED) fit alone.

Parameter	Units	Value
M_*	Mass (M$_\odot$)	$0.350^{+0.024}_{-0.028}$
R_*	Radius (R$_\odot$)	$0.342^{+0.011}_{-0.011}$
ρ_*	Density (cgs)	$12.2^{+1.2}_{-1.1}$
log g	Surface gravity (cgs)	$4.912^{+0.031}_{-0.033}$
L_*	Luminosity (L$_\odot$)	$0.01381^{+0.00048}_{-0.00043}$
$F_{\rm bol}$	Bolometric flux (cgs 10^{-10})	$3.98^{+0.14}_{-0.12}$
$T_{\rm eff}$	Effective temperature (K)	3383^{+52}_{-54}
[Fe/H]	Metallicity (dex)	$0.15^{+0.10}_{-0.10}$
A_V	V-band extinction (mag)	$0.070^{+0.090}_{-0.052}$
$\sigma_{\rm SED}$	SED photometry error scaling	$1.9^{+0.74}_{-0.45}$
ϖ	Parallax (mas)	$29.997^{+0.057}_{-0.057}$
d	Distance (pc)	$33.337^{+0.064}_{-0.063}$

3.2 Galactic component

Combined with the tangential velocity (μ_α, μ_δ) and the stellar parallax (ϖ) from *Gaia* EDR3 and the spectroscopically determined systemic RV from the SpeX spectrum, we calculate the three-dimensional space motion with respect to the local standard of rest (LSR) based on the methodology described in Johnson & Soderblom (1987). We obtain three-dimensional space velocities $U_{\rm LSR} = -25.15 \pm 2.26$ km s^{-1}, $V_{\rm LSR} = -9.42 \pm 5.27$ km s^{-1}, $W_{\rm LSR} = 13.16 \pm 1.75$ km s^{-1}, respectively. We further identify the Galactic population membership of TOI-2136 following the criterion first used in Bensby, Feltzing & Lundström (2003). We compute a relative probability $P_{\rm thick}/P_{\rm thin} = 0.01$, indicating a thin-disc origin. Finally, we integrate the stellar orbit with the 'MWPotential2014' Galactic potential using GALPY (Bovy 2015) following the procedure described in Gan et al. (2020), and we estimate that the maximal height $Z_{\rm max}$ of TOI-2136 above the Galactic plane is about 206 pc. Therefore, we conclude that TOI-2136 belongs to the thin-disc population, which is also consistent with its solar-like metallicity.

3.3 Stellar activity and rotation period

Stellar activity, often manifesting as stellar rotation signals, is expected to affect the RV measurements and makes it challenging to accurately determine the planet mass (Queloz et al. 2009; Howard et al. 2013; Pepe et al. 2013), especially when its time-scale is close to the planet orbital period (Gan et al. 2021). In order to evaluate the effect of the stellar activity on the RVs, we first search for the periodic signals in the *TESS* PDCSAP light curve after masking the known in-transit data using the generalized Lomb–Scargle (GLS) periodogram (Zechmeister & Kürster 2009), and we find no signs of stellar variation. However, we note that the PDCSAP photometry from *TESS* flattens variability on time-scales greater than about 15 d and *TESS* is insensitive to long-term stellar rotational features due to its sector-by-sector observational strategy. Thus, we further examine the archival long-term photometric time series data from ground-based surveys. We look into the rotational modulation of TOI-2136 in the publicly available light curve taken by the Zwicky Transient Facility (ZTF; Masci et al. 2019). A total of 1054 measurements were acquired in r band spanning 1112 d. After removing the observations flagged as bad quality, we have 1011 measurements left with a standard deviation of 0.011 mag. We compute the GLS periodogram and find a clear peak at 75 ± 5 d (see Fig. 7), which is consistent with the estimation of $P_{\rm rot} \sim 82.97$ d derived by Newton

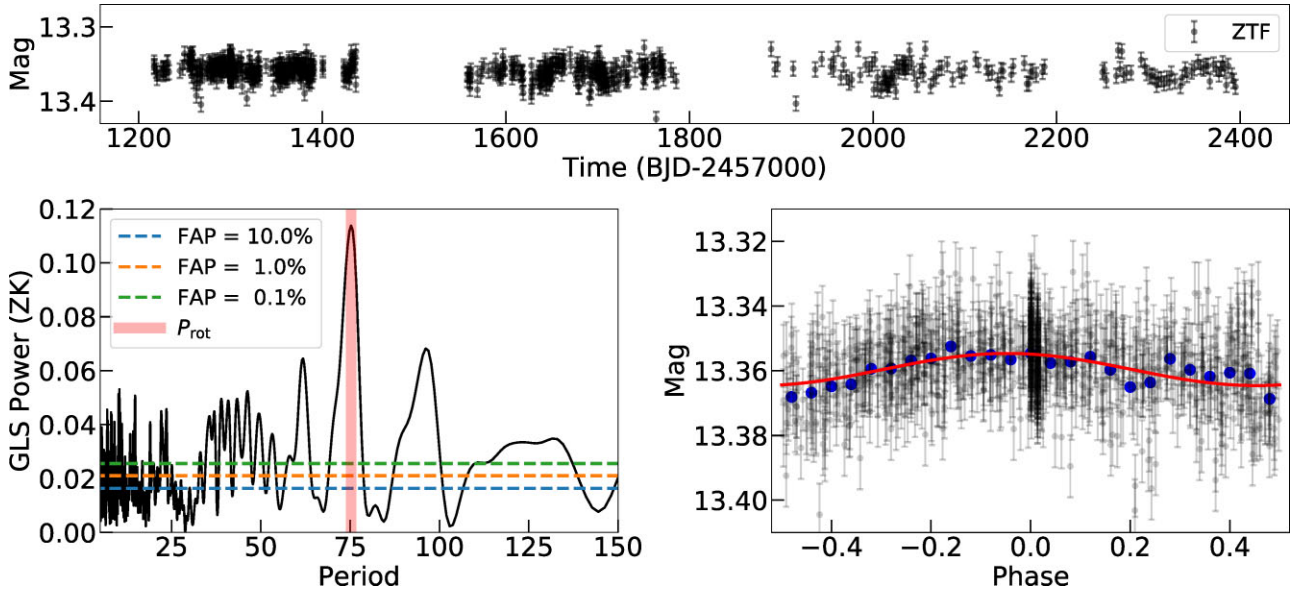

Figure 7. Top panel: the ground-based long-term light curve of TOI-2136 taken by ZTF. Bottom left-hand panel: the GLS periodogram of the ZTF photometry. The vertical red line represents the ∼75 d rotational signal of TOI-2136. The theoretical false alarm probability (FAP) levels of 10 per cent, 1 per cent, and 0.1 per cent are marked as horizontal lines with different colours. Bottom right-hand panel: the phase-folded ZTF light curve at 75 d along with the best-fitting sinusoidal model, shown as a red solid curve. The blue dots are the binned data.

et al. (2016) using the data from MEarth (Nutzman & Charbonneau 2008). To test the significance of this 75-d signal and search for potential aliases in the window function, we adopted the bootstrap method, randomly reassigning flux values from the ZTF photometry to the observed epochs to generate an artificial (shuffled) light curve. We repeated the process 10 000 times and ran the same GLS analysis. We find that only 1.5 per cent of the bootstrapped light curves have a maximum peak located within 75 ± 5 d. Additionally, the lack of significant flaring activity in the *TESS* light curves also suggests that the host star is quiet and inactive. We thus attribute this 75 ± 5 d signal to the stellar rotation. Adopting the empirical relations from Engle & Guinan (2018), we estimate that TOI-2136 has an age of 4.6 ± 1.0 Gyr, consistent with our thin-disc population conclusion.

4 ANALYSIS AND RESULTS

In this section, we outline our data analysis steps including modelling the space and ground light curves and the SPIRou RVs, which mainly follows Gan et al. (2022). In short, we begin with fitting the *TESS*-only photometry and then take the posterior information as a prior to detrend the ground-based light curves (see Section 4.1). We next perform a pre-analysis to the RVs and test the significance of eccentricity (see Section 4.2), and we carry out a joint fit of all data to obtain the best-fitting physical parameters of TOI-2136 b (see Section 4.3). Finally, we conduct a transit timing variation (TTV) analysis to look for potential evidence of another non-transiting planet (see Section 4.4).

4.1 Photometric analysis

4.1.1 TESS only

We first employ the JULIET package (Espinoza, Kossakowski & Brahm 2019) to fit the detrended *TESS* light curve, which makes use of BATMAN (Kreidberg 2015) to build the transit model and DYNESTY (Higson et al. 2019; Speagle 2020) to carry out dynamic nested sampling and determine the Bayesian posteriors of system parameters. Instead of fitting the planet-to-star radius ratio ($p = R_p/R_*$) and the impact parameter $b = a\cos i/R_*$ directly, JULIET utilizes the new parametrizations r_1 and r_2 to make the sampling more efficient as it focuses on physically meaningful values of a transiting system with $0 < b < 1 + p$ (Espinoza 2018). We carry out a circular-orbit fit with $e = 0$. Consequently, the left degrees of freedom are r_1, r_2, mid-transit epoch T_0, orbital period P_b, and stellar density ρ_*. We place uniform priors on both T_0 and P_b according to the outputs from our transit least-squares analysis, and allow r_1 and r_2 to vary uniformly between 0 and 1. Regarding the stellar density, we impose a non-informative log-uniform prior. We fit two limb-darkening coefficients under the triangular sampling scheme (i.e. q_1 and q_2; Kipping 2013), and adopt uniform priors on both of them. In addition, we also include an extra flux jitter term to account for additional systematics, on which we set a wide log-uniform prior. We do not take light contamination into account here. The prior settings and the median along with 1σ credible intervals of transit parameter's posteriors are given in Table B1.

In order to investigate the potential evidence of orbital eccentricity from the photometric-only data, we rerun our fit with free e and w and compare the Bayesian model log-evidence ($\ln Z$) difference between the circular and eccentric models. Basically, JULIET considers that a model is significantly favoured if it has a $\ln Z$ improvement over 5 and moderately supported if $\Delta \ln Z > 2.5$ based on the criteria described in Trotta (2008). We find that the circular orbit model is slightly preferred with a Bayesian evidence improvement of $\Delta \ln Z = \ln Z_{\rm Circular} - \ln Z_{\rm Eccentric} = 1.1$. Therefore, we conclude that no significant orbital eccentricity preference is shown in the *TESS* data.

4.1.2 Ground-based photometry

Since parts of ground light curves show obvious linear coherence between flux and time, we perform a uniform detrending using GP

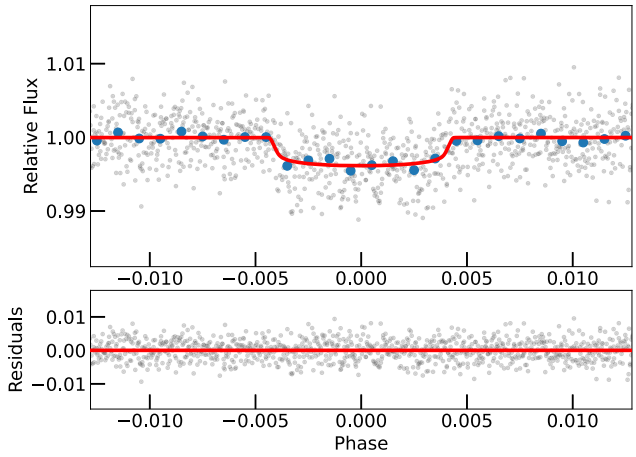

Figure 8. The *TESS* light curve folded in phase with the orbital period of TOI-2136 b. The red solid line represents the best-fitting transit model from the final joint fit (see Section 4.3). The blue dots are the binned data of every phase interval of 0.001. The residuals are plotted below.

regressors with the CELERITE Matérn-3/2 kernel to remove systematic trends. Rather than mask out the in-transit data and interpolate to renormalize the light curve as stated in Section 2.1, here we perform a simultaneous GP+transit fit to all ground data given their short out-of-transit span. We fit a single transit model but independent GP models for each ground data set. We take the posteriors from the previous circular orbit fit, and put informative priors on P_b, T_0, r_1, r_2, and ρ_*. Regarding the GP hyperparameters ρ_{GP} and σ_{GP}, we place wide log-uniform priors on both of them. We show our prior adoption and posteriors in Table B2, and present our raw and reprocessed ground light curves in Fig. 3.

4.2 RV analysis

We perform an RV-only fit using JULIET, which employs the RADVEL package (Fulton et al. 2018) to model the Keplerian RV signals. Since the expected RVs caused by the planet perturbation are expected to be small, we choose to fix the orbital period P_b and mid-transit epoch $T_{0,b}$ at the best-fitting transit ephemeris derived from the *TESS*-only fit to avoid introducing additional uncertainties. As the *TESS* photometric data do not show evidence for eccentricity, we first assume a circular orbit and fix eccentricity e at 0, and the argument of periastron ω at 90°. Moreover, we do not take the RV slope $\dot{\gamma}$ or the quadratic trend $\ddot{\gamma}$ into consideration and fix them at zero due to the short time span of our RV data. We include a simple jitter term σ_{RV} that is added in quadrature to the error bars of each data point to account for an extra white noise. We set uniform priors on both the RV semi-amplitude K_b and the systemic velocity μ but a log-uniform prior on σ_{RV}. We obtain $K_b = 4.1 \pm 1.5$ m s^{-1}, which is consistent with the expected value ~3.7 m s^{-1} supposing a planet mass estimated using the mass–radius relation from Chen & Kipping (2017).

In order to test the significance of the RV detection, we rerun the RV fit but with a flat model. We find the planet model described above is favoured but not statistically significant with a Bayesian evidence improvement of $\Delta \ln Z = \ln Z_{Planet} - \ln Z_{Flat} = 2.0$. Finally, we construct a Keplerian model with free e and ω to look for the significance of eccentricity in the RV data. We find that the circular orbit model is slightly preferred with a Bayesian evidence improvement of $\Delta \ln Z = \ln Z_{Circular} - \ln Z_{Eccentric} = 1.2$, agreeing with our findings in the *TESS* photometric data (see Section 4.1.1).

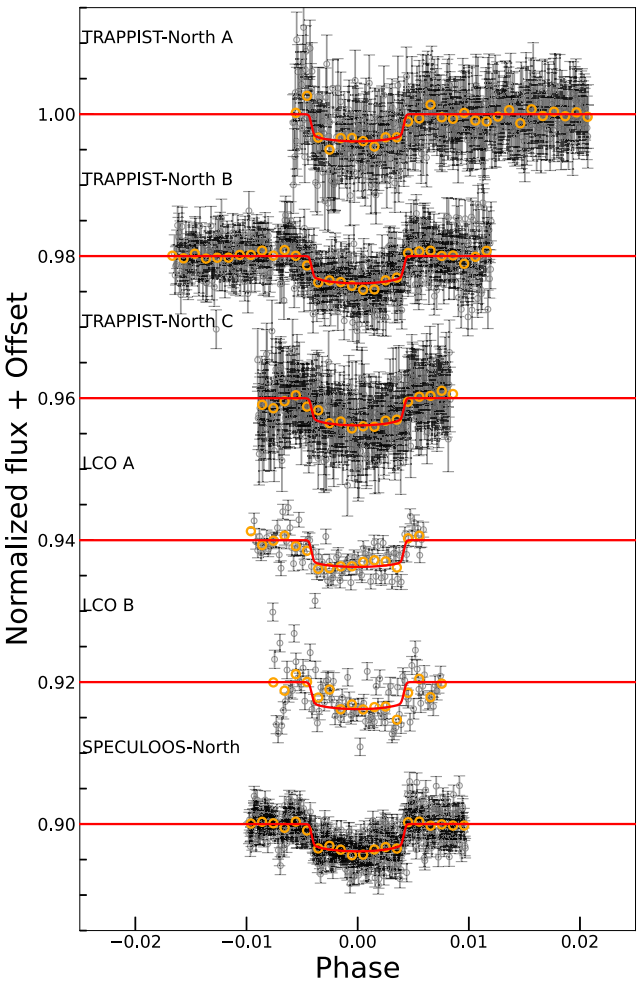

Figure 9. All ground-based photometry phase folded on the best-fitting orbital period of TOI-2136 b with arbitrary offsets. The red solid lines are the median transit models from the final joint fit (see Section 4.3). The overplotted orange circles are the binned data every phase interval of 0.001.

4.3 Joint fit

Building on the results from the independent transit and RV fits, we finally carry out a joint fit using JULIET to simultaneously model all detrended space and ground light curves together with the SPIRou RVs to infer the properties of the TOI-2136 b. We place the same priors as we did in Section 4.1.1 except that: (1) we adopt Gaussian priors for the linear limb-darkening coefficients of the ground-based light curves, centred at the estimates from the LDTK package (Husser et al. 2013; Parviainen & Aigrain 2015) with a 1σ value of 0.1; (2) we fit a dilution factor for the *TESS* photometry to account for possible light contamination that has not been fully corrected by PDC. As there is less contamination in the ground data, we fix all dilution factors D_i to 1. For the RV part, we use the same priors as in Section 4.2. The phase-folded *TESS* and ground light curves along with the best-fitting transit models are shown in Figs 8 and 9. The RV time series and the best-fitting RV model are presented in Fig. 10. The fitted RV semi-amplitude is 4.2 ± 1.4 m s^{-1}, a detection close to a 3σ significance. Our joint-fit model reveals that the planet has a radius of 2.20 ± 0.17 R$_\oplus$ with a mass of 6.37 ± 2.45 M$_\oplus$. All priors and the median of the posterior distributions for each fitted parameter are summarized in Table 4. The posterior distributions of key parameters are presented in Fig. C1. We also run a separate joint

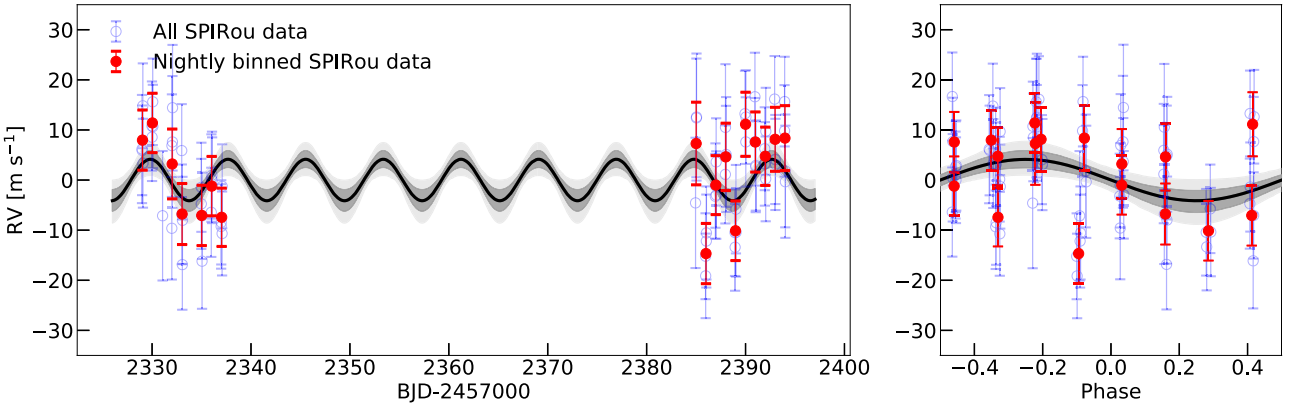

Figure 10. Left-hand panel: time series of the SPIRou RVs after subtracting the best-fitting systemic velocity. The blue circles are all original SPIRou data taken every night while the red dots are the nightly binned RVs. The black solid line is the median RV model from the final joint fit (see Section 4.3). The grey shaded areas denote the 1σ and 2σ credible intervals of the RV model. Right-hand panel: phase-folded SPIRou RVs. The presented RV error bars in both panels are the quadrature sum of the fitted instrument jitter and the measurement uncertainties.

fit using EXOFASTV2 (Eastman et al. 2019), and we verify that similar results were obtained within 1σ.

4.4 Transit timing variation

We search for the transit timing variations (TTVs) with all the photometric data sets (*TESS*, LCOGT, TRAPPIST-North, and SPECULOOS-North) using EXOFASTV2. EXOFASTV2 uses the Differential Evolution Markov chain Monte Carlo method to derive the values and their uncertainties of the stellar and planetary parameters of the system. It fits a linear ephemeris to the transit times and adds a penalty for the deviation of the step's linear ephemeris from the best-fitting linear ephemeris of the transit times. For the TTV analysis of TOI-2136 b, we fix the stellar parameters to the values in Table 1 and orbital parameters to the results obtained from the joint-fit performed. The results of the analysis showing the difference between the observed transit times and the calculated linear ephemeris from all the transits is presented in Fig. 11. We find no evidence of a significant TTV signal in the current photometric data.

4.5 Statistical validation

Since the mass constraint on the planet has a significance slightly below 3σ, we make use of the TRICERATOPS package (Giacalone et al. 2021) to vet and statistically validate the planetary nature of TOI-2136 b. TRICERATOPS is a Bayesian tool that takes host and nearby stars into consideration and calculate the probabilities of different transit-producing scenarios. The output false positive probability (FPP) value quantifies the possibility that the transit signal is not due to a planet around the host star. We first apply TRICERATOPS to the *TESS* light curve along with the contrast curve obtained by the 'Alopeke speckle imaging (832 nm). The resulting FPP value 0.014 is close to the normal FPP threshold of 0.015 (1.5 per cent) to classify a validated planet (Giacalone et al. 2021). Wells et al. (2021) found that ground light curves sometimes put a better photometric constraint than the *TESS* data. We thus rerun the pipeline using the same contrast curve but the SPECULOOS-North/Artemis time series, which yields a FPP value of 4×10^{-3}. Therefore, we consider this TOI to be a validated planet.

5 DISCUSSION

5.1 Composition of TOI-2136 b

We use the radius constraint on TOI-2136 b derived from the transit photometry and the measured mass from the SPIRou RV data to investigate the location of this planet in the mass–radius diagram. Fig. 12 shows the mass and radius distribution of a sample of well-characterized planets with the precisions on both measurements better than 30 per cent taken from the TEPcat data base (Southworth 2011). The composition curves are retrieved from Zeng, Sasselov & Jacobsen (2016). The mass and radius of TOI-2136 b are compared to the two-layer internal structure models of Zeng et al. (2016). As can be seen from Fig. 12, TOI-2136 b appears to have a composition consistent with a pure water-ice world or a rocky planet with moderate atmosphere.

We further investigate the composition of TOI-2136 b using the Exoplanet Composition Interpolator.[5] The algorithm takes the planet evolution models proposed by Lopez & Fortney (2014) and interpolates between the grid of these pre-computed models to explore the interiors and compositions of the planets. Taking the planet mass, radius, insolation flux, and stellar age as inputs, we find the rocky core and gaseous envelope of TOI-2136 b have mass fractions of $98.7^{+1.0}_{-1.5}$ per cent and $1.3^{+1.5}_{-1.0}$ per cent, respectively.

5.2 TOI-2136 b and radius valley

The bimodality of radius distribution shown in small planets around FGK stars, which splits them into super-Earths and sub-Neptunes, is known as a transition between planets with and without extended gaseous envelopes (Fulton et al. 2017; Fulton & Petigura 2018). Martinez et al. (2019) found that this transition radius is orbital period dependent, following a power law of $r_{\rm p,\,valley} \propto P^{-0.11}$. This finding approximately agrees with the prediction from the thermally driven atmospheric mass-loss scenarios including photoevaporation and core-powered envelope escape ($r_{\rm p,\,valley} \propto P^{-0.15}$; Lopez & Rice 2018). However, observational results from Cloutier & Menou (2020) suggested that the transition radius of small planets around M dwarfs is likely in accordance with the gas-poor formation model (Lee et al.

[5]https://tools.emac.gsfc.nasa.gov/ECI/

Table 4. Parameter priors and the best-fitting values along with the 68 per cent credibility intervals in the final joint fit for TOI-2136. $\mathcal{N}(\mu\ ,\ \sigma^2)$ means a normal prior with mean μ and standard deviation σ. $\mathcal{U}(a, b)$ stands for a uniform prior ranging from a to b. $\mathcal{J}(a, b)$ stands for a Jeffrey's prior ranging from a to b.

Parameter	Prior	Best fit	Description
Planetary parameters			
$P_{\rm b}$ (d)	$\mathcal{U}$ (7.6, 8.0)	$7.85193^{+0.000019}_{-0.000016}$	Orbital period of TOI-2136 b
$T_{0,\,\rm b}$ (BJD – 245 7000)	$\mathcal{U}$ (2014, 2020)	$2017.7042^{+0.0009}_{-0.0010}$	Mid-transit time of TOI-2136 b
$r_{1,\,\rm b}$	$\mathcal{U}$ (0, 1)	$0.55^{+0.07}_{-0.08}$	Parametrization for p and b
$r_{2,\,\rm b}$	$\mathcal{U}$ (0, 1)	$0.0596^{+0.0010}_{-0.0009}$	Parametrization for p and b
$e_{\rm b}$	0	Fixed	Orbital eccentricity of TOI-2136 b
$\omega_{\rm b}$ (°)	90	Fixed	Argument of periapsis of TOI-2136 b
Photometry parameters			
$D_{\rm TESS}$	$\mathcal{N}$ (0.85^a, 0.1^2)	$0.91^{+0.05}_{-0.04}$	Dilution factor of *TESS* photometry
$M_{\rm TESS}$	$\mathcal{N}$ (0, 0.1^2)	$-0.000001^{+0.000019}_{-0.000018}$	Mean out-of-transit flux of *TESS* photometry
$\sigma_{\rm TESS}$ (ppm)	$\mathcal{J}$ (10^{-6}, 10^6)	$0.01^{+1.94}_{-0.01}$	*TESS* additive photometric jitter term
q_1	$\mathcal{U}$ (0, 1)	$0.32^{+0.27}_{-0.17}$	Quadratic limb-darkening coefficient of *TESS* photometry
q_2	$\mathcal{U}$ (0, 1)	$0.31^{+0.31}_{-0.20}$	Quadratic limb-darkening coefficient of *TESS* photometry
$D_{\rm all}$	Fixed	1	Dilution factors of ground photometry
$M_{\rm TRAPPIST\text{-}North,\,A}$	$\mathcal{N}$ (0, 0.1^2)	$-0.00011^{+0.00019}_{-0.00017}$	Mean out-of-transit flux of TRAPPIST-North-A photometry
$\sigma_{\rm TRAPPIST\text{-}North,\,A}$ (ppm)	$\mathcal{J}$ (0.1, 10^5)	$7.9^{+85.2}_{-6.3}$	Additive photometric jitter term of TRAPPIST-North-A photometry
$q_{\rm TRAPPIST\text{-}North,\,A}$	$\mathcal{N}$ (0.31, 0.1^2)	$0.31^{+0.08}_{-0.08}$	Linear limb-darkening coefficient of TRAPPIST-North-A photometry
$M_{\rm TRAPPIST\text{-}North,\,B}$	$\mathcal{N}$ (0, 0.1^2)	$-0.00005^{+0.00011}_{-0.00011}$	Mean out-of-transit flux of TRAPPIST-North-B photometry
$\sigma_{\rm TRAPPIST\text{-}North,\,B}$ (ppm)	$\mathcal{J}$ (0.1, 10^5)	$8.6^{+120.9}_{-8.1}$	Additive photometric jitter term of TRAPPIST-North-B photometry
$q_{\rm TRAPPIST\text{-}North,\,B}$	$\mathcal{N}$ (0.31, 0.1^2)	$0.34^{+0.08}_{-0.09}$	Linear limb-darkening coefficient of TRAPPIST-North-B photometry
$M_{\rm TRAPPIST\text{-}North,\,C}$	$\mathcal{N}$ (0, 0.1^2)	$-0.00008^{+0.00024}_{-0.00022}$	Mean out-of-transit flux of TRAPPIST-North-C photometry
$\sigma_{\rm TRAPPIST\text{-}North,\,C}$ (ppm)	$\mathcal{J}$ (0.1, 10^5)	$7.6^{+91.3}_{-7.1}$	Additive photometric jitter term of TRAPPIST-North-C photometry
$q_{\rm TRAPPIST\text{-}North,\,C}$	$\mathcal{N}$ (0.31, 0.1^2)	$0.32^{+0.08}_{-0.09}$	Linear limb-darkening coefficient of TRAPPIST-North-C photometry
$M_{\rm LCO\text{-}CTIO,\,A}$	$\mathcal{N}$ (0, 0.1^2)	$-0.00007^{+0.00019}_{-0.00018}$	Mean out-of-transit flux of LCO-CTIO-A photometry
$\sigma_{\rm LCO\text{-}CTIO,\,A}$ (ppm)	$\mathcal{J}$ (0.1, 10^5)	$1534.7^{+158.5}_{-143.1}$	Additive photometric jitter term of LCO-CTIO-A photometry
$q_{\rm LCO\text{-}CTIO,\,A}$	$\mathcal{N}$ (0.31, 0.1^2)	$0.27^{+0.08}_{-0.08}$	Linear limb-darkening coefficient of LCO-CTIO-A photometry
$M_{\rm LCO\text{-}CTIO,\,B}$	$\mathcal{N}$ (0, 0.1^2)	$-0.00009^{+0.00028}_{-0.00029}$	Mean out-of-transit flux of LCO-CTIO-B photometry
$\sigma_{\rm LCO\text{-}CTIO,\,B}$ (ppm)	$\mathcal{J}$ (0.1, 10^5)	$2729.3^{+227.6}_{-228.5}$	Additive photometric jitter term of LCO-CTIO-B photometry
$q_{\rm LCO\text{-}CTIO,\,B}$	$\mathcal{N}$ (0.31, 0.1^2)	$0.32^{+0.07}_{-0.07}$	Linear limb-darkening coefficient of LCO-CTIO-B photometry
$M_{\rm SPECULOOS\text{-}North}$	$\mathcal{N}$ (0, 0.1^2)	$-0.00005^{+0.00009}_{-0.00009}$	Mean out-of-transit flux of SPECULOOS-North photometry
$\sigma_{\rm SPECULOOS\text{-}North}$ (ppm)	$\mathcal{J}$ (0.1, 10^5)	$1534.4^{+82.9}_{-77.8}$	Additive photometric jitter term of SPECULOOS-North photometry
$q_{\rm SPECULOOS\text{-}North}$	$\mathcal{N}$ (0.31, 0.1^2)	$0.32^{+0.06}_{-0.07}$	Linear limb-darkening coefficient of SPECULOOS-North photometry
Stellar parameters			
ρ_* (kg m^{-3})	$\mathcal{J}$ (10^3, 10^5)	14208^{+1717}_{-2114}	Stellar density
RV parameters			
$K_{\rm b}$ (m s^{-1})	$\mathcal{U}$ (0, 30)	$4.2^{+1.4}_{-1.4}$	RV semi-amplitude of TOI-2136 b
$\mu_{\rm SPIRou}$ (m s^{-1})	$\mathcal{U}$ (−29 100, −29 000)	$-29067.2^{+1.0}_{-1.1}$	Systemic velocity for SPIRou
$\sigma_{\rm SPIRou}$ (m s^{-1})	$\mathcal{J}$ (0.1, 100)	$4.4^{+1.4}_{-1.5}$	Extra jitter term for SPIRou
Derived parameters			
$R_{\rm p}/R_*$		$0.0596^{+0.0010}_{-0.0009}$	Planet radius in units of stellar radius
$R_{\rm p}$ ($R_\oplus$)		$2.20^{+0.17}_{-0.17}$	Planet radius
$M_{\rm p}$ ($M_\oplus$)		$6.37^{+2.45}_{-2.29}$	Planet mass
$\rho_{\rm p}$ (g cm^{-3})		$3.29^{+2.55}_{-1.63}$	Planet density
b		$0.34^{+0.11}_{-0.13}$	Impact parameter
a/R_*		$35.91^{+1.40}_{-1.87}$	Semimajor axis in units of stellar radii
a (au)		$0.057^{+0.005}_{-0.005}$	Semimajor axis
i (°)		$89.4^{+0.2}_{-0.2}$	Inclination angle
$S_{\rm p}$ ($S_\oplus$)		$4.0^{+2.1}_{-1.5}$	Insolation flux relative to the Earth
$T_{\rm eq}$ [b] (K)		394^{+20}_{-19}	Equilibrium temperature

[a]This initial guess is taken from the contamination ratio reported in *TESS* Input Catalog version 8 (TICv8; (Stassun et al. 2019).
[b]We set an albedo $A_{\rm B} = 0$ here and assume there is no heat distribution between the dayside and nightside.

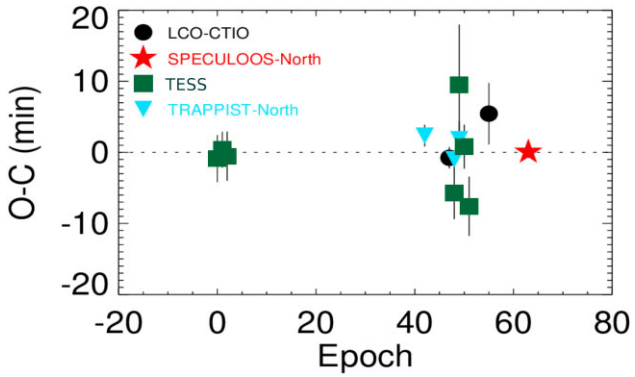

Figure 11. The transit timing variations (TTVs) of TOI-2136 as a function of epoch number. No significant TTV signal was detected.

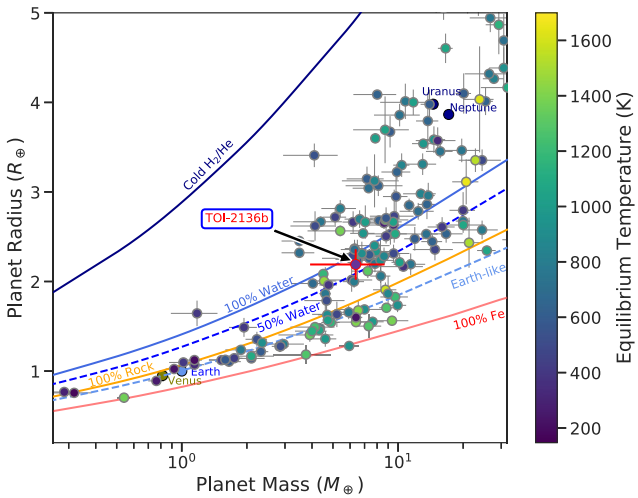

Figure 12. Mass–radius curves with planets colour coded by their surface temperatures, indicating the potential bulk compositions of TOI-2136 b. Data are taken from the TEPCat data base of well-characterized planets. Theoretical models for the planet's internal composition are taken from Zeng et al. (2016).

2014; Lee & Chiang 2016), following $r_{\rm p,\,valley} \propto P^{0.11}$. For early-type M dwarfs with mass around 0.64 $M_\odot$, Cloutier et al. (2020) found that the thermally driven atmospheric mass-loss scenario remains efficient at sculpting their close-in planets. Recent work from Luque et al. (2021) tentatively reached a different conclusion. They proposed that the planetary radius valley for stars within a mass range between 0.54 and 0.64 $M_\odot$ probably results from gas-poor formation. The relative dominance of these competing physical processes at the low stellar mass end remains unclear. Thus, populating the number of small planets with known bulk composition is crucial to solve the puzzles.

Fig. 13 shows the orbital period and radius of planets with mass determination around M dwarfs ($M_* \lesssim 0.65$ $M_\odot$). We can see that *TESS* has doubled the number of small planets with known density, making them important for further investigating the strength of the two aforementioned envelope escape physical processes. With a period of $P_{\rm b} = 7.85$ d and a radius of $R_{\rm p} = 2.20 \pm 0.17$ $R_\oplus$, TOI-2136 b is located slightly above the radius valley for M dwarfs predicted by the thermally driven atmospheric mass-loss model (see Fig. 13). Theoretical studies infer that TOI-2136 b should be

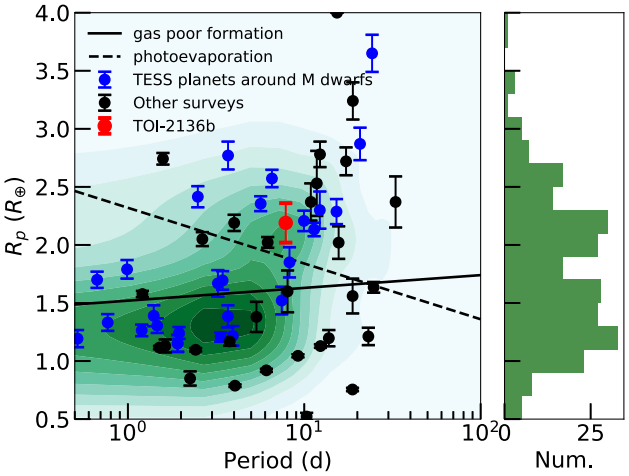

Figure 13. The planet radius and orbital period diagram of all confirmed small planets hosted by M stars ($M_* \lesssim 0.65$ $M_\odot$). The green contours are the density distribution of planets without mass measurements. The 1 d radius distribution is shown on the right. The coloured points are the planets with mass constraint from TTV or RV. Especially, the blue dots are planets detected by the *TESS* mission. The solid and dashed lines depict the locations of radius valley for M stars predicted by the gas-poor and photoevaporation models, taken from Cloutier & Menou (2020). TOI-2136 b is marked as a red dot.

predominantly gaseous. Indeed, our previous analysis shows that TOI-2136 b likely retains a H/He envelope with a small mass fraction. Given an estimated stellar age of 4.6 ± 1.0 Gyr, TOI-2136 has, in principle, finished the photoevaporation stage, which has a time-scale of hundreds of Myr (Owen & Wu 2013, 2017). However, it is possible that TOI-2136 is still undergoing the mass-loss process following the core-powered mechanism that has a Gyr time-scale (Ginzburg et al. 2018).

Another interesting question is the behaviour of the radius valley as a function of stellar mass. Both competing physical processes predict a positive correlation between the centre of radius valley and stellar mass, although different models show a difference in the slope at each mass bin (Lopez & Rice 2018; Gupta & Schlichting 2019; Wu 2019). Consequently, comparing the theoretical predictions with the observational findings may rule out certain models. Cloutier & Menou (2020) obtained a similar positive trend using a subsample of *Kepler* and *K2* planets. However, the sample size is small, especially for planets around mid-to-late M dwarfs, leading to a relatively large statistical uncertainty. Nevertheless, TOI-2136 b joins the small but growing sample of planets around mid-M dwarfs that may help understand evolution of the transition radius with stellar mass in the future.

5.3 Prospects for future observations

Given the proximity and small size, TOI-2136 is a promising star for atmospheric studies. Following the criteria proposed in Kempton et al. (2018), we compute the transmission spectroscopy metric (TSM) of TOI-2136 b based on the stellar and planet radius, planet mass, equilibrium temperature, and the apparent magnitude of the host star in the J band to examine its potential opportunities for atmospheric characterization with the *James Webb Space Telescope* (*JWST*; Gardner et al. 2006). We derive a TSM of 65^{+20}_{-32} for TOI-2136 b. We compare the TSM factor of TOI-2136 b with other small planets ($R_{\rm p} \leq 4$ $R_\oplus$) harboured around M dwarfs ($M_* \leq 0.65$ $M_\odot$)

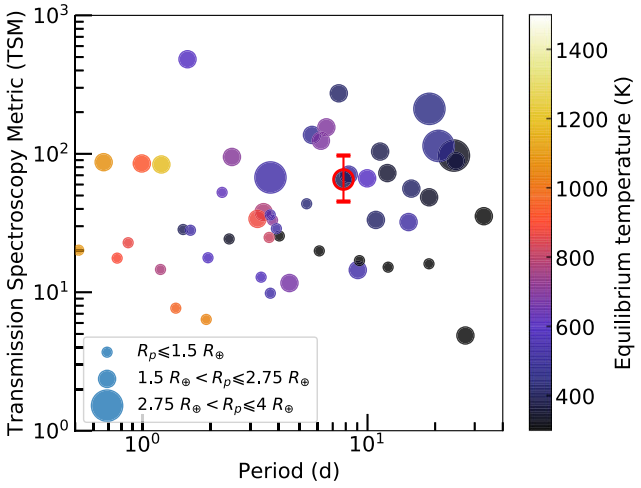

Figure 14. The transmission spectroscopy metric as a function of orbital period for small planets around M dwarfs ($M_* \lesssim 0.65$ M$_\odot$), coloured by the planet equilibrium temperature. TOI-2136 b is shown as a dot surrounded by a red circle with error bars. The size of each point is proportional to the planet radius.

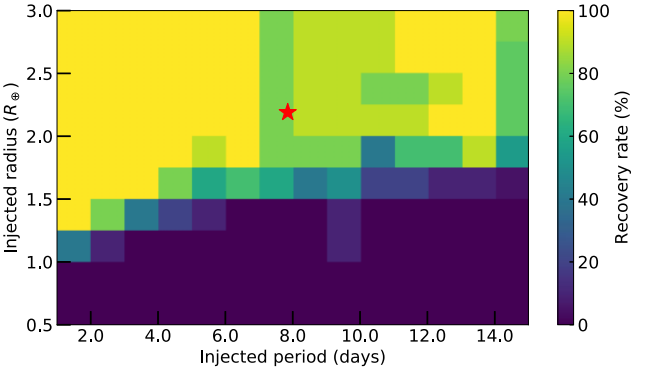

Figure 15. The results of injection-and-recovery test on the *TESS* light curve of TOI-2136. We search the P–R_p space with 10 random generated mid-transit times for each grid and we explore a total of 1680 scenarios. Different colours represent different recovery rates. The yellow and green regions are the planetary parameter space with high recovery rate, while the planets located in the dark regions may be missed. The red star marks the position of TOI-2136 b.

with mass measurements from RVs or TTVs in Fig. 14. Kempton et al. (2018) quantified TSM = 90 as a recommended threshold for planets with $1.5 < R_p < 10$ R$_\oplus$ to be high-quality atmospheric characterization targets. Thus, TOI-2136 b is located close to the first rank of targets with a relatively low equilibrium temperature T_{eq}. In addition, we also estimate the signal amplitude of TOI-2136 b in the transit transmission spectroscopy following the approach described in Gillon et al. (2016):

$$S = \frac{2R_p h_{eff}}{R_*^2}, \quad (1)$$

where R_p and R_* are the planet and its host star radius and h_{eff} is the effective atmospheric height. We calculate the signal amplitude under the typical case that $h_{eff}/H = 7$, where $H = kT/\mu g$ is the atmospheric scale height. We find an S of 382 ± 196 ppm, assuming a bond albedo of 0 and a mean molecular mass μ of 2.3 amu for sub-Neptunes (Demory et al. 2020). The large uncertainty mainly comes from the loose constraint on the planet mass. Schlawin et al. (2020) reported a noise floor level 10 ppm for *JWST* for NIRSpec ($\lambda = 5.0$–11 μm). Our S measurement for TOI-2136 b is between 19 and 58 times this noise floor. Taking these two aspects into consideration, we suggest that TOI-2136 b is an exciting target for further atmospheric researches. A number of studies on the diversity of sub-Neptunian atmospheres have already been made (e.g. Lavvas et al. 2019; Chouqar et al. 2020).

As noted above, the mean molecular mass μ is degenerated with the surface gravity of the planet (i.e. planet mass M_p). Thus, a well-measured planet mass is required to fully understand the compositions of the planet atmosphere. Otherwise, the accuracy and precision of the retrieved atmospheric parameters will be largely limited (Batalha et al. 2019). Since the current SPIRou RVs only provide a 2σ mass constraint and TOI-2136 is a quiet M dwarf without strong stellar activity, future subsequent spectroscopy observations are encouraged to determine the planet mass at the 3σ confidence level and look for other potential non-transiting planets. Because of the faintness of TOI-2136 ($V_{mag} = 14.3$), it challenges most optical spectroscopy instruments on the ground. However, it is still accessible by NIR facilities like InfraRed Doppler (IRD) spectrograph (Kotani et al. 2018) and Habitable-zone Planet Finder (HPF; Mahadevan et al. 2014) or red-optical spectrographs on large telescopes like MAROON-X (Seifahrt et al. 2018), which is dedicated to conducting RV measurements for mid-to-late M dwarfs.

5.4 Detection limits

Based on the results from the *Kepler* survey, Muirhead et al. (2015) found that 21^{+7}_{-5} per cent of mid-M dwarf stars like TOI-2136 host compact multiple planets with periods all shorter than 10 d. This rate is not very different from that of early-type M dwarfs but much higher than solar-like stars. Therefore, we perform an injection-and-recovery test using MATRIX TOOLKIT[6] (Demory et al. 2020; Pozuelos et al. 2020) to explore the detection limits of the current *TESS* data and determine the type of planets we perhaps miss. We make use of all available PDCSAP light curves of TOI-2136 after removing the known transits of TOI-2136 b. We explore a period–radius space of 1–15 d and 0.5–3.0 R$_\oplus$ with step sizes of 1 d and 0.25 R$_\oplus$. During the injection, we assume that the synthetic 'planet' has an inclination of $i = 90°$ on a circular orbit, and randomly generate 10 light curves with different T_0 for each grid. We thus examine a total of 1680 scenarios. For each light curve, we use a biweight filter with a window size of 0.5 d to remove the systematic trends. MATRIX TOOLKIT defines a successful recovery if the detected period is within 5 per cent of the injected period and the transit duration is within 1 h when compared with the set value. Fig. 15 depicts our test results. We find that: (1) most planets smaller than super-Earths ($R_p \lesssim 1.5$ R$_\oplus$) across the period range we searched are likely to be still buried in the light curve and remain undetectable (Brady & Bean 2021); (2) planets that have $R_p \gtrsim 2.0$ R$_\oplus$ with periods up to 15 d can be ruled out with a recovery rate $\geq$80 per cent. Since the current *TESS* data set is insensitive to planets with period larger than 15 d, here we note that future *TESS* observations to be done in Sectors 53 and 54 between 2022 June 13 and 2022 August 5 during the extended mission would help better understand the architecture of this system.

6 CONCLUSION

We report the discovery and characterization of the TOI-2136 system, a sub-Neptune around a faint M4.5 dwarf ($V = 14.1$ mag), detected

[6]https://github.com/PlanetHunters/tkmatrix

by the *TESS* mission. We confirm the planetary nature of TOI-2136 b through a combination of 2-min cadence *TESS* observations, ground-based photometry, high angular resolution imaging, and SPIRou spectroscopic observations. The transit and RV joint-fit model gives a planet radius of $R_{\rm p} = 2.20^{+0.17}_{-0.17}\,{\rm R}_{\oplus}$, a mass of $M_{\rm p} = 6.37^{+2.45}_{-2.29}\,{\rm M}_{\oplus}$, and an equilibrium temperature of $T_{\rm eq} = 395^{+24}_{-22}$ K. The bulk density $\rho_{\rm p} = 3.29^{+2.55}_{-1.63}$ g cm^{-3} of TOI-2136 b is consistent with a water world or a rocky planet with moderate atmosphere. Planetary structure models of TOI-2136 b suggest that it may contain a rocky core with a H/He envelope with a mass fraction of $1.3^{+1.5}_{-1.0}$ per cent. Given the period and radius of TOI-2136 b, it falls close to the location of radius valley predicted by the thermally driven envelope escape model for M dwarfs, making it an excellent laboratory to investigate the formation and evolution models of small planets around M dwarfs. The small size and quiet nature of the host star and its brightness in the NIR make TOI-2136 b amenable for observation by most *JWST* modes for studying atmospheric compositions.

ACKNOWLEDGEMENTS

We are grateful to Coel Hellier for the insights regarding the WASP data. We thank Ryan Cloutier for useful discussions. We also thank Elise Furlan for the contributions to the speckle data. This work is partly supported by the National Science Foundation of China (Grant Nos 11390372, 11761131004, and 12133005 to SM and TG). ASo was supported by a grant from the MOBILE 2 BE project, coordinated by the University of Porto in the framework of the European Programme Erasmus plus. BVR thanks the Heising-Simons Foundation for support. YGMC is supported by UNAM-PAPIIT-IG101321. CXH's work is supported by ARC DECRA Grant. ODSD is supported in the form of work contract (DL 57/2016/CP1364/CT0004) funded by FCT. This research uses data obtained through the China's Telescope Access Program (TAP), which has been funded by the TAP member institutes. This work uses observations obtained with SPIRou, an international project led by Institut de Recherche en Astrophysique et Planetologie, Toulouse, France. The authors wish to recognize and acknowledge the very significant cultural role and reverence that the summit of Maunakea has always had within the indigenous Hawaiian community. We are most fortunate to have the opportunity to conduct observations from this mountain. We further acknowledge that Lick Observatory sits on the unceded ancestral homelands of the Chochenyo and Tamyen Ohlone peoples, including the Alson and Socostac tribes, who were the original inhabitants of the area that includes Mt. Hamilton. This publication benefits from the support of the French Community of Belgium in the context of the FRIA Doctoral Grant awarded to MT. The research leading to these results has received funding from the ARC grant for Concerted Research Actions, financed by the Federation Wallonia-Brussels. TRAPPIST is funded by the Belgian Fund for Scientific Research (Fond National de la Recherche Scientifique, FNRS) under the grant PDR T.0120.21. TRAPPIST-North is a project funded by the University of Liège (Belgium), in collaboration with Cadi Ayyad University of Marrakech (Morocco). MG and EJ are F.R.S.-FNRS Senior Research Associate. CL is supported by the National Science Foundation Graduate Research Fellowship under Grant No. DGE1745303. Some of the observations in the paper made use of the High-Resolution Imaging instrument 'Alopeke obtained under Gemini LLP Proposal Number: GN/S-2021A-LP-105. 'Alopeke was funded by the NASA Exoplanet Exploration Program and built at the NASA Ames Research Center by Steve B. Howell, Nic Scott, Elliott P. Horch, and Emmett Quigley. 'Alopeke was mounted on the Gemini North (and/or South) telescope of the international Gemini Observatory, a program of NSF's OIR Lab, which is managed by the Association of Universities for Research in Astronomy (AURA) under a cooperative agreement with the National Science Foundation on behalf of the Gemini partnership: the National Science Foundation (United States), National Research Council (Canada), Agencia Nacional de Investigación y Desarrollo (Chile), Ministerio de Ciencia, Tecnología e Innovación (Argentina), Ministério da Ciência, Tecnologia, Inovações e Comunicações (Brazil), and Korea Astronomy and Space Science Institute (Republic of Korea). This work makes use of observations from the LCOGT network. Part of the LCOGT telescope time was granted by NOIRLab through the Mid-Scale Innovations Program (MSIP). MSIP is funded by NSF. The ULiege's contribution to SPECULOOS has received funding from the European Research Council under the European Union's Seventh Framework Programme (FP/2007-2013) (grant agreement no. 336480/SPECULOOS), from the Balzan Prize Foundation, from the Belgian Scientific Research Foundation (F.R.S. - FNRS; grant no. T.0109.20), from the University of Liège, and from the ARC grant for Concerted Research Actions financed by the Federation Wallonia-Brussels. LD is an F.R.S. - FNRS Post-doctoral Researcher. VVG is F.R.S - FNRS Research Associate. This work is supported by a grant from the Simons Foundation (PI: Queloz, grant number 327127). JdW and MT gratefully acknowledge financial support from the Heising-Simons Foundation, Dr Colin Masson, and Dr Peter A. Gilman for Artemis, the first telescope of the SPECULOOS network situated in Tenerife, Spain. MNG acknowledges support from the European Space Agency (ESA) as an ESA Research Fellow. This work is supported by the Swiss National Science Foundation (PP00P2-163967, PP00P2-190080 and the National Centre for Competence in Research PlanetS). This work has received fund from the European Research Council (ERC) under the European Union's Horizon 2020 Framework Programme (grant agreement no. 803193/BEBOP), from the MERAC Foundation, and from the Science and Technology Facilities Council (STFC; grant no. ST/S00193X/1). This work was supported by Fundação para a Ciência e a Tecnologia (FCT) and Fundo Europeu de Desenvolvimento Regional (FEDER) via COMPETE2020 through the research grants UIDB/04434/2020, UIDP/04434/2020, PTDC/FIS-AST/32113/2017, POCI-01-0145-FEDER-032113, PTDC/FIS-AST/28953/2017, and POCI-01-0145-FEDER-028953. The National Geographic Society – Palomar Observatory Sky Atlas (POSS-I) was made by the California Institute of Technology with grants from the National Geographic Society. Funding for the *TESS* mission is provided by NASA Science Mission Directorate. We acknowledge the use of *TESS* public data from pipelines at the *TESS* Science Office and at the *TESS* Science Processing Operations Center. Resources supporting this work were provided by the NASA High-End Computing (HEC) Program through the NASA Advanced Supercomputing (NAS) Division at Ames Research Center for the production of the SPOC data products. This research has made use of the Exoplanet Follow-up Observation Program website, which is operated by the California Institute of Technology, under contract with the National Aeronautics and Space Administration under the Exoplanet Exploration Program. This paper includes data collected by the *TESS* mission, which are publicly available from the Mikulski Archive for Space Telescopes (MAST). This work has made use of data from the European Space Agency (ESA) mission *Gaia* (https://www.cosmos.esa.int/gaia), processed by the *Gaia* Data Processing and Analysis Consortium (DPAC, https://www.cosmos.esa.int/web/gaia/dpac/consortium). Funding for the DPAC has been provided by national institutions,

in particular the institutions participating in the *Gaia* Multilateral Agreement. This work made use of TPFPLOTTER by J. Lillo-Box (publicly available in www.github.com/jlillo/tpfplotter), which also made use of the PYTHON packages ASTROPY, LIGHTKURVE, MATPLOTLIB, and NUMPY.

Based on observations obtained at the Canada–France–Hawaii Telescope (CFHT) that is operated by the National Research Council (NRC) of Canada, the Institut National des Sciences de l'Univers of the Centre National de la Recherche Scientifique (CNRS) of France, and the University of Hawaii. The observations at the CFHT were performed with care and respect from the summit of Maunakea that is a significant cultural and historic site.

DATA AVAILABILITY

This paper includes photometric data collected by the *TESS* mission and ground instruments, which are publicly available in ExoFOP, at https://exofop.ipac.caltech.edu/tess/target.php?id = 336128819. All spectroscopy data underlying this paper are listed in the Appendix. All of the high-resolution speckle imaging data are available at the NASA Exoplanet Archive with no proprietary period.

REFERENCES

Abell G. O., 1955, PASP, 67, 258
Agol E. et al., 2021, Planet. Sci. J., 2, 1
Aller A., Lillo-Box J., Jones D., Miranda L. F., Barceló Forteza S., 2020, A&A, 635, A128
Artigau É. et al., 2014, in Peck A. B., Benn C. R., Seaman R. L., eds, Proc. SPIE Vol. 9149, Observatory Operations: Strategies, Processes, and Systems V. SPIE, Bellingham, p. 914905
Artigau É. et al., 2021, AJ, 162, 144
Baranec C. et al., 2014, ApJ, 790, L8
Barkaoui K. et al., 2019, AJ, 157, 43
Batalha N. E., Lewis T., Fortney J. J., Batalha N. M., Kempton E., Lewis N. K., Line M. R., 2019, ApJ, 885, L25
Benedict G. F. et al., 2016, AJ, 152, 141
Bensby T., Feltzing S., Lundström I., 2003, A&A, 410, 527
Borucki W. J. et al., 2010, Science, 327, 977
Bouchy F., Pepe F., Queloz D., 2001, A&A, 374, 733
Bovy J., 2015, ApJS, 216, 29
Boyajian T. S., van Belle G., von Braun K., 2014, AJ, 147, 47
Brady M., Bean J., 2021, preprint (arXiv:2112.08337)
Brown T. M. et al., 2013, PASP, 125, 1031
Cersullo F., Wildi F., Chazelas B., Pepe F., 2017, A&A, 601, A102
Charbonneau D. et al., 2009, Nature, 462, 891
Chen J., Kipping D., 2017, ApJ, 834, 17
Chen H., Rogers L. A., 2016, ApJ, 831, 180
Choi J., Dotter A., Conroy C., Cantiello M., Paxton B., Johnson B. D., 2016, ApJ, 823, 102
Chouqar J., Benkhaldoun Z., Jabiri A., Lustig-Yaeger J., Soubkiou A., Szentgyorgyi A., 2020, MNRAS, 495, 962
Ciardi D. R., Beichman C. A., Horch E. P., Howell S. B., 2015, ApJ, 805, 16
Cloutier R., Menou K., 2020, AJ, 159, 211
Cloutier R. et al., 2020, AJ, 160, 22
Collins K. A., Kielkopf J. F., Stassun K. G., Hessman F. V., 2017, AJ, 153, 77
Cristofari P. I. et al., 2022, MNRAS, 511, 1893
Cushing M. C., Vacca W. D., Rayner J. T., 2004, PASP, 116, 362
Cutri R. M. et al., 2003, The IRSA 2MASS All-Sky Point Source Catalog. NASA/IPAC Infrared Science Archive, Available at:http://irsa.ipac.caltech.edu/applications/Gator/
Delrez L. et al., 2018, in Marshall H. K., Spyromilio J., eds, Proc. SPIE Vol. 10700, Ground-based and Airborne Telescopes VII. SPIE, Bellingham, p. 107001I
Demory B. O. et al., 2020, A&A, 642, A49
Donati J. F. et al., 2020, MNRAS, 498, 5684
Dotter A., 2016, ApJS, 222, 8
Eastman J. D. et al., 2019, preprint (arXiv:1907.09480)
Engle S. G., Guinan E. F., 2018, Res. Notes Am. Astron. Soc., 2, 34
Espinoza N., 2018, Res. Notes Am. Astron. Soc., 2, 209
Espinoza N., Kossakowski D., Brahm R., 2019, MNRAS, 490, 2262
Foreman-Mackey D., Agol E., Ambikasaran S., Angus R., 2017, AJ, 154, 220
Fressin F. et al., 2013, ApJ, 766, 81
Fukui A. et al., 2021, AJ, 162, 167
Fulton B. J., Petigura E. A., 2018, AJ, 156, 264
Fulton B. J. et al., 2017, AJ, 154, 109
Fulton B. J., Petigura E. A., Blunt S., Sinukoff E., 2018, PASP, 130, 044504
Furlan E., Howell S. B., 2017, AJ, 154, 66
Furlan E., Howell S. B., 2020, ApJ, 898, 47
Gaia Collaboration et al., 2018, A&A, 616, A1
Gaia Collaboration et al., 2021, A&A, 649, A1
Gan T. et al., 2020, AJ, 159, 160
Gan T. et al., 2021, MNRAS, 501, 6042
Gan T. et al., 2022, MNRAS, 511, 83
Garcia L. J., Timmermans M., Pozuelos F. J., Ducrot E., Gillon M., Delrez L., Wells R. D., Jehin E., 2022, MNRAS, 509, 4817
Gardner J. P. et al., 2006, Space Sci. Rev., 123, 485
Gavel D. et al., 2014, in Marchetti E., Close L. M., Véran J.-P., eds, Proc. SPIE Vol. 9148, Adaptive Optics Systems IV. SPIE, Bellingham, p. 914805
Giacalone S. et al., 2021, AJ, 161, 24
Gillon M., Jehin E., Magain P., Chantry V., Hutsemékers D., Manfroid J., Queloz D., Udry S., 2011, in Bouchy F., Díaz R., Moutou C., eds, EPJ Web Conf. Vol. 11, Detection and Dynamics of Transiting Exoplanets. EDP Sciences, Les Ulis, France, p. 06002
Gillon M. et al., 2016, Nature, 533, 221
Ginzburg S., Schlichting H. E., Sari R., 2018, MNRAS, 476, 759
Gupta A., Schlichting H. E., 2019, MNRAS, 487, 24
Gupta A., Schlichting H. E., 2020, MNRAS, 493, 792
Gupta A., Schlichting H. E., 2021, MNRAS, 504, 4634
Higson E., Handley W., Hobson M., Lasenby A., 2019, Stat. Comput., 29, 891
Hippke M., Heller R., 2019, A&A, 623, A39
Hobson M. J. et al., 2021, A&A, 648, A48
Howard A. W. et al., 2012, ApJS, 201, 15
Howard A. W. et al., 2013, Nature, 503, 381
Howell S. B., Everett M. E., Sherry W., Horch E., Ciardi D. R., 2011, AJ, 142, 19
Howell S. B. et al., 2014, PASP, 126, 398
Howell S. B., Everett M. E., Horch E. P., Winters J. G., Hirsch L., Nusdeo D., Scott N. J., 2016, ApJ, 829, L2
Howell S. B., Matson R. A., Ciardi D. R., Everett M. E., Livingston J. H., Scott N. J., Horch E. P., Winn J. N., 2021, AJ, 161, 164
Husser T. O., Wende-von Berg S., Dreizler S., Homeier D., Reiners A., Barman T., Hauschildt P. H., 2013, A&A, 553, A6
Jehin E. et al., 2011, The Messenger, 145, 2
Jenkins J. M., 2002, ApJ, 575, 493
Jenkins J. M. et al., 2016, in Chiozzi G., Guzman J. C., eds, Proc. SPIE Vol. 9913, Software and Cyberinfrastructure for Astronomy IV. SPIE, Bellingham, p. 99133E
Jenkins J. M., Tenenbaum P., Seader S., Burke C. J., McCauliff S. D., Smith J. C., Twicken J. D., Chandrasekaran H., 2020, Technical Report, Kepler Science Document KSCI-19081-003. NASA Ames Research Center, Moffett Field, CA, id. 9
Jensen E., 2013, Astrophysics Source Code Library, record ascl:1306.007
Jensen-Clem R., Duev D. A., Riddle R., Salama M., Baranec C., Law N. M., Kulkarni S. R., Ramprakash A. N., 2018, AJ, 155, 32
Jin S., Mordasini C., Parmentier V., van Boekel R., Henning T., Ji J., 2014, ApJ, 795, 65
Johnson D. R. H., Soderblom D. R., 1987, AJ, 93, 864
Johnson J. A. et al., 2017, AJ, 154, 108
Kempton E. M. R. et al., 2018, PASP, 130, 114401

Kipping D. M., 2013, MNRAS, 435, 2152
Klein B. et al., 2021, MNRAS, 502, 188
Kotani T. et al., 2018, in Evans C. J., Simard L., Takami H., eds, Proc. SPIE Vol. 10702, Ground-based and Airborne Instrumentation for Astronomy VII. SPIE, Bellingham, p. 1070211
Kreidberg L., 2015, PASP, 127, 1161
Kupke R. et al., 2012, in Ellerbroek B. L., Marchetti E., Véran J.-P., eds, Proc. SPIE Vol. 8447, Adaptive Optics Systems III. SPIE, Bellingham, p. 84473G
Lamman C. et al., 2020, AJ, 159, 139
Lavvas P., Koskinen T., Steinrueck M. E., García Muñoz A., Showman A. P., 2019, ApJ, 878, 118
Lee E. J., Chiang E., 2016, ApJ, 817, 90
Lee E. J., Chiang E., Ormel C. W., 2014, ApJ, 797, 95
Lester K. V. et al., 2021, AJ, 162, 75
Li J., Tenenbaum P., Twicken J. D., Burke C. J., Jenkins J. M., Quintana E. V., Rowe J. F., Seader S. E., 2019, PASP, 131, 024506
Lopez E. D., Fortney J. J., 2014, ApJ, 792, 1
Lopez E. D., Rice K., 2018, MNRAS, 479, 5303
Luque R. et al., 2019, A&A, 628, A39
Luque R. et al., 2021, A&A, 645, A41
McCully C., Volgenau N. H., Harbeck D.-R., Lister T. A., Saunders E. S., Turner M. L., Siiverd R. J., Bowman M., 2018, in Guzman J. C., Ibsen J., eds, Proc. SPIE Vol. 10707, Software and Cyberinfrastructure for Astronomy V. SPIE, Bellingham, p. 107070K
McGurk R. et al., 2014, in Marchetti E., Close L. M., Vran J.-P., eds, Proc. SPIE Vol. 9148, Adaptive Optics Systems IV. SPIE, Bellingham, p. 91483A
Mahadevan S. et al., 2014, in Ramsay S. K., McLean I. S., Takami H., eds, Proc. SPIE Vol. 9147, Ground-based and Airborne Instrumentation for Astronomy V. SPIE, Bellingham, p. 91471G
Mann A. W., Brewer J. M., Gaidos E., Lépine S., Hilton E. J., 2013, AJ, 145, 52
Mann A. W., Feiden G. A., Gaidos E., Boyajian T., von Braun K., 2015, ApJ, 804, 64
Mann A. W. et al., 2019, ApJ, 871, 63
Martinez C. F., Cunha K., Ghezzi L., Smith V. V., 2019, ApJ, 875, 29
Martioli E. et al., 2022, A&A, 660, A86
Masci F. J. et al., 2019, PASP, 131, 018003
Ment K. et al., 2019, AJ, 157, 32
Morris R. L., Twicken J. D., Smith J. C., Clarke B. D., Jenkins J. M., Bryson S. T., Girouard F., Klaus T. C., 2020, Technical Report, Kepler Science Document KSCI-19081-003. NASA Ames Research Center, Moffett Field, CA, id. 6
Moutou C. et al., 2020, A&A, 642, A72
Muirhead P. S. et al., 2015, ApJ, 801, 18
Newton E. R., Charbonneau D., Irwin J., Berta-Thompson Z. K., Rojas-Ayala B., Covey K., Lloyd J. P., 2014, AJ, 147, 20
Newton E. R., Irwin J., Charbonneau D., Berta-Thompson Z. K., Dittmann J. A., West A. A., 2016, ApJ, 821, 93
Niraula P. et al., 2020, AJ, 160, 172
Nutzman P., Charbonneau D., 2008, PASP, 120, 317
Owen J. E., Wu Y., 2013, ApJ, 775, 105
Owen J. E., Wu Y., 2017, ApJ, 847, 29
Parviainen H., Aigrain S., 2015, MNRAS, 453, 3821
Pepe F. et al., 2013, Nature, 503, 377
Petigura E. A., Howard A. W., Marcy G. W., 2013, Proc. Natl. Acad. Sci., 110, 19273
Petigura E. A. et al., 2017, AJ, 154, 107
Pozuelos F. J. et al., 2020, A&A, 641, A23
Queloz D. et al., 2009, A&A, 506, 303
Rayner J. T., Toomey D. W., Onaka P. M., Denault A. J., Stahlberger W. E., Vacca W. D., Cushing M. C., Wang S., 2003, PASP, 115, 362
Rayner J. T., Cushing M. C., Vacca W. D., 2009, ApJS, 185, 289
Ricker G. R. et al., 2015, J. Astron. Telesc. Instrum. Syst., 1, 014003
Savel A. B., Dressing C. D., Hirsch L. A., Ciardi D. R., Fleming J. P. C., Giacalone S. A., Mayo A. W., Christiansen J. L., 2020, AJ, 160, 287
Schlafly E. F., Finkbeiner D. P., 2011, ApJ, 737, 103
Schlawin E., Leisenring J., Misselt K., Greene T. P., McElwain M. W., Beatty T., Rieke M., 2020, AJ, 160, 231
Scott N. J. et al., 2021, Frontiers Astron. Space Sci., 8, 138
Sebastian D. et al., 2021, A&A, 645, A100
Seifahrt A., Stürmer J., Bean J. L., Schwab C., 2018, in Evans C. J., Simard L., Takami H., eds, Proc. SPIE Vol. 10702, Ground-based and Airborne Instrumentation for Astronomy VII. SPIE, Bellingham, p. 107026D
Shporer A. et al., 2020, ApJ, 890, L7
Smith J. C. et al., 2012, PASP, 124, 1000
Soto M. G. et al., 2021, A&A, 649, A144
Southworth J., 2011, MNRAS, 417, 2166
Speagle J. S., 2020, MNRAS, 493, 3132
Stassun K. G. et al., 2018, AJ, 156, 102
Stassun K. G. et al., 2019, AJ, 158, 138
Stumpe M. C. et al., 2012, PASP, 124, 985
Stumpe M. C., Smith J. C., Catanzarite J. H., Van Cleve J. E., Jenkins J. M., Twicken J. D., Girouard F. R., 2014, PASP, 126, 100
Trotta R., 2008, Contemporary Phys., 49, 71
Twicken J. D., Clarke B. D., Bryson S. T., Tenenbaum P., Wu H., Jenkins J. M., Girouard F., Klaus T. C., 2010, in Radziwill N. M., Bridger A., eds, Proc. SPIE Vol. 7740, Software and Cyberinfrastructure for Astronomy. SPIE, Bellingham, p. 774023
Twicken J. D. et al., 2018, PASP, 130, 064502
Vanderspek R. et al., 2019, ApJ, 871, L24
Van Eylen V., Agentoft C., Lundkvist M. S., Kjeldsen H., Owen J. E., Fulton B. J., Petigura E., Snellen I., 2018, MNRAS, 479, 4786
Wells R. D. et al., 2021, A&A, 653, A97
Wright E. L. et al., 2010, AJ, 140, 1868
Wu Y., 2019, ApJ, 874, 91
Zechmeister M., Kürster M., 2009, A&A, 496, 577
Zeng L., Sasselov D. D., Jacobsen S. B., 2016, ApJ, 819, 127
Ziegler C., Tokovinin A., Briceño C., Mang J., Law N., Mann A. W., 2020, AJ, 159, 19

APPENDIX A: SPIROU RVS

Table A1. SPIRou RV measurements of TOI-2136. Each observation took an exposure time of 900 s.

BJD_{TDB}	RV (m s^{-1})	σ_{RV} (m s^{-1})
245 9328.981	−29061.14	9.74
245 9328.992	−29061.40	7.65
245 9329.065	−29052.51	7.08
245 9329.076	−29063.97	7.55
245 9329.987	−29056.56	7.60
245 9329.997	−29058.77	7.42
245 9330.065	−29051.71	7.27
245 9330.075	−29056.66	6.92
245 9331.060	−29074.46	12.06
245 9331.995	−29076.96	9.11
245 9332.006	−29060.47	9.12
245 9332.057	−29059.73	12.31
245 9332.068	−29052.90	11.65
245 9332.997	−29061.45	8.02
245 9333.008	−29074.18	8.81
245 9333.059	−29084.22	7.70
245 9333.070	−29075.37	7.33
245 9334.975	−29072.09	7.69
245 9334.986	−29068.77	7.58
245 9335.051	−29083.52	8.29
245 9335.062	−29074.47	7.25
245 9335.985	−29073.77	7.59
245 9335.995	−29066.93	7.38

Table A1 – *continued*

BJD_{TDB}	RV ($m\ s^{-1}$)	σ_{RV} ($m\ s^{-1}$)
245 9336.058	−29066.35	7.32
245 9336.069	−29067.37	7.19
245 9336.983	−29076.59	7.03
245 9336.993	−29075.78	7.01
245 9337.077	−29078.00	6.97
245 9337.088	−29068.59	6.97
245 9384.944	−29071.89	12.14
245 9384.955[a]	−29028.67	12.07
245 9385.032	−29054.93	10.89
245 9385.042	−29054.76	11.79
245 9385.956	−29082.54	7.20
245 9385.967	−29086.46	7.04
245 9386.035	−29079.50	8.03
245 9386.046	−29077.88	8.04
245 9386.947	−29070.58	7.05
245 9386.958	−29068.43	7.02
245 9387.028	−29063.71	7.36
245 9387.039	−29070.33	7.40
245 9387.961	−29066.21	8.62
245 9387.971	−29056.82	11.73
245 9388.026	−29062.60	8.94
245 9388.037	−29062.24	10.48
245 9388.935	−29077.83	7.29
245 9388.946	−29080.74	7.34
245 9389.029	−29073.15	7.51
245 9389.040	−29077.78	7.51
245 9389.933[a]	−29035.46	7.34
245 9389.944	−29054.10	7.19
245 9390.026	−29059.72	7.61
245 9390.037	−29054.76	8.11
245 9390.949	−29050.71	7.46
245 9390.959	−29059.70	7.41
245 9391.028	−29064.68	7.78
245 9391.039	−29064.43	7.71
245 9391.944	−29061.08	6.85
245 9391.955	−29064.11	6.92
245 9392.037	−29067.10	7.07
245 9392.048	−29057.61	7.34
245 9392.929[a]	−29037.53	7.37
245 9392.940	−29051.17	7.23
245 9393.009	−29063.23	7.58
245 9393.020	−29064.21	7.82
245 9393.943	−29057.52	7.87
245 9393.954	−29051.67	7.65
245 9394.016	−29065.51	10.25
245 9394.027	−29067.68	10.18

[a]The data points are outliers, which were removed during the RV analysis.

APPENDIX B: PRIOR SETTINGS FOR *TESS*-ONLY FIT AND GROUND PHOTOMETRIC DATA DETRENDING

Table B1. Prior settings and posterior values for the fit to the *TESS*-only data.

Parameter	Best fit	Prior	Description
Planetary parameters			
$P_{\rm b}$ (d)	$7.85192^{+0.0005}_{-0.0005}$	$\mathcal{U}$ (7.6, 8.0)	Orbital period of TOI-2136 b
$T_{0,\,\rm b}$ (BJD – 245 7000)	$2017.7039^{+0.0013}_{-0.0015}$	$\mathcal{U}$ (2014, 2020)	Mid-transit time of TOI-2136 b
$r_{1,\,\rm b}$	$0.599^{+0.083}_{-0.067}$	$\mathcal{U}$ (0, 1)	Parametrization for p and b
$r_{2,\,\rm b}$	$0.058^{+0.002}_{-0.002}$	$\mathcal{U}$ (0, 1)	Parametrization for p and b
$e_{\rm b}$	0	Fixed	Orbital eccentricity of TOI-2136 b
$\omega_{\rm b}$ (°)	90	Fixed	Argument of periapsis of TOI-2136 b
Stellar parameters			
ρ_* (kg m^{-3})	12721^{+1573}_{-1789}	$\mathcal{J}$ (10^3, 10^5)	Stellar density
TESS photometry parameters			
$D_{\rm TESS}$	1	Fixed	*TESS* photometric dilution factor
$M_{\rm TESS}$	$0.00002^{+0.00001}_{-0.00001}$	$\mathcal{N}$ (0, 0.1^2)	Mean out-of-transit flux of *TESS* photometry
$\sigma_{\rm TESS}$ (ppm)	$0.03^{+4.62}_{-0.02}$	$\mathcal{J}$ (10^{-6}, 10^6)	*TESS* additive photometric jitter term
q_1	$0.37^{+0.36}_{-0.23}$	$\mathcal{U}$ (0, 1)	Quadratic limb-darkening coefficient
q_2	$0.31^{+0.32}_{-0.20}$	$\mathcal{U}$ (0, 1)	Quadratic limb-darkening coefficient

Table B2. Prior settings and posterior values of the GP+transit fit to detrend all ground-based photometry.

Parameter	Best fit	Prior	Description
Planetary parameters			
$P_{\rm b}$ (d)	$7.85193^{+0.00002}_{-0.00002}$	$\mathcal{U}$ (7.84, 7.86)	Orbital period of TOI-2136 b
$T_{0,\,\rm b}$ (BJD – 245 7000)	$2017.7042^{+0.0012}_{-0.0013}$	$\mathcal{U}$ (2017.699, 2017.709)	Mid-transit time of TOI-2136 b
$r_{1,\,\rm b}$	$0.65^{+0.02}_{-0.03}$	$\mathcal{U}$ (0.4, 0.8)	Parametrization for p and b
$r_{2,\,\rm b}$	$0.0598^{+0.0011}_{-0.0012}$	$\mathcal{U}$ (0.05, 0.07)	Parametrization for p and b
$e_{\rm b}$	0	Fixed	Orbital eccentricity of TOI-2136 b
$\omega_{\rm b}$ (°)	90	Fixed	Argument of periapsis of TOI-2136 b
Stellar parameters			
ρ_* (kg m^{-3})	11254^{+201}_{-187}	$\mathcal{N}$ (12 721, 1789^2)	Stellar density
Photometry parameters			
D_i	1	Fixed	Photometric dilution factors for all ground photometry
$M_{\rm TRAPPIST\text{-}North,\,A}$	$-0.001^{+0.016}_{-0.013}$	$\mathcal{N}$ (0, 0.1^2)	Mean out-of-transit flux of TRAPPIST-North-A photometry
$\sigma_{\rm TRAPPIST\text{-}North,\,A}$ (ppm)	$6.6^{+79.1}_{-6.1}$	$\mathcal{J}$ (10^{-1}, 10^5)	Additive photometric jitter term of TRAPPIST-North-A photometry
$q_{\rm TRAPPIST\text{-}North,\,A}$	$0.59^{+0.23}_{-0.27}$	$\mathcal{U}$ (0, 1)	Linear limb-darkening coefficient of TRAPPIST-North-A photometry
$M_{\rm TRAPPIST\text{-}North,\,B}$	$-0.021^{+0.026}_{-0.063}$	$\mathcal{N}$ (0, 0.1^2)	Mean out-of-transit flux of TRAPPIST-North-B photometry
$\sigma_{\rm TRAPPIST\text{-}North,\,B}$ (ppm)	$57.1^{+210.2}_{-51.3}$	$\mathcal{J}$ (10^{-1}, 10^5)	Additive photometric jitter term of TRAPPIST-North-B photometry
$q_{\rm TRAPPIST\text{-}North,\,B}$	$0.55^{+0.17}_{-0.21}$	$\mathcal{U}$ (0, 1)	Linear limb-darkening coefficient of TRAPPIST-North-B photometry
$M_{\rm TRAPPIST\text{-}North,\,C}$	$-0.001^{+0.015}_{-0.005}$	$\mathcal{N}$ (0, 0.1^2)	Mean out-of-transit flux of TRAPPIST-North-C photometry
$\sigma_{\rm TRAPPIST\text{-}North,\,C}$ (ppm)	$5.2^{+55.4}_{-4.7}$	$\mathcal{J}$ (10^{-1}, 10^5)	Additive photometric jitter term of TRAPPIST-North-C photometry
$q_{\rm TRAPPIST\text{-}North,\,C}$	$0.54^{+0.18}_{-0.21}$	$\mathcal{U}$ (0, 1)	Linear limb-darkening coefficient of TRAPPIST-North-C photometry
$M_{\rm LCO\text{-}CTIO,\,A}$	$0.004^{+0.029}_{-0.017}$	$\mathcal{N}$ (0, 0.1^2)	Mean out-of-transit flux of LCO-CTIO-A photometry
$\sigma_{\rm LCO\text{-}CTIO,\,A}$ (ppm)	$1539.3^{+145.2}_{-122.7}$	$\mathcal{J}$ (10^{-1}, 10^5)	Additive photometric jitter term of LCO-CTIO-A photometry
$q_{\rm LCO\text{-}CTIO,\,A}$	$0.22^{+0.17}_{-0.13}$	$\mathcal{U}$ (0, 1)	Linear limb-darkening coefficient of LCO-CTIO-A photometry
$M_{\rm LCO\text{-}CTIO,\,B}$	$0.001^{+0.019}_{-0.009}$	$\mathcal{N}$ (0, 0.1^2)	Mean out-of-transit flux of LCO-CTIO-B photometry
$\sigma_{\rm LCO\text{-}CTIO,\,B}$ (ppm)	$2708.4^{+181.7}_{-186.5}$	$\mathcal{J}$ (10^{-1}, 10^5)	Additive photometric jitter term of LCO-CTIO-B photometry
$q_{\rm LCO\text{-}CTIO,\,B}$	$0.49^{+0.23}_{-0.23}$	$\mathcal{U}$ (0, 1)	Linear limb-darkening coefficient of LCO-CTIO-B photometry
$M_{\rm SPECULOOS\text{-}North}$	$-0.007^{+0.018}_{-0.037}$	$\mathcal{N}$ (0, 0.1^2)	Mean out-of-transit flux of SPECULOOS-North photometry
$\sigma_{\rm SPECULOOS\text{-}North}$ (ppm)	$1533.1^{+61.1}_{-63.8}$	$\mathcal{J}$ (10^{-1}, 10^5)	Additive photometric jitter term of SPECULOOS-North photometry
$q_{\rm SPECULOOS\text{-}North}$	$0.40^{+0.15}_{-0.15}$	$\mathcal{U}$ (0, 1)	Linear limb-darkening coefficient of SPECULOOS-North photometry
GP parameters			
$\rho_{\rm TRAPPIST\text{-}North,\,A}$	$46.9^{+53.7}_{-44.9}$	$\mathcal{J}$ (10^{-6}, 10^6)	GP time-scale of the TRAPPIST-North-A photometry
$\sigma_{\rm TRAPPIST\text{-}North,\,A}$	$0.017^{+0.073}_{-0.014}$	$\mathcal{J}$ (10^{-6}, 10^6)	GP amplitude of the TRAPPIST-North-A photometry

Table B2 – *continued*

Parameter	Best fit	Prior	Description
$\rho_{\mathrm{TRAPPIST\text{-}North,\,B}}$	$6.8^{+43.8}_{-5.4}$	$\mathcal{J}\,(10^{-6}, 10^{6})$	GP time-scale of the TRAPPIST-North-B photometry
$\sigma_{\mathrm{TRAPPIST\text{-}North,\,B}}$	$0.063^{+0.355}_{-0.047}$	$\mathcal{J}\,(10^{-6}, 10^{6})$	GP amplitude of the TRAPPIST-North-B photometry
$\rho_{\mathrm{TRAPPIST\text{-}North,\,C}}$	$52.7^{+34.5}_{-50.2}$	$\mathcal{J}\,(10^{-6}, 10^{6})$	GP time-scale of the TRAPPIST-North-C photometry
$\sigma_{\mathrm{TRAPPIST\text{-}North,\,C}}$	$0.009^{+0.036}_{-0.007}$	$\mathcal{J}\,(10^{-6}, 10^{6})$	GP amplitude of the TRAPPIST-North-C photometry
$\rho_{\mathrm{LCO\text{-}CTIO,\,A}}$	$1317.4^{+1568.2}_{-1299.4}$	$\mathcal{J}\,(10^{-6}, 10^{6})$	GP time-scale of the LCO-CTIO-A photometry
$\sigma_{\mathrm{LCO\text{-}CTIO,\,A}}$	$0.039^{+0.115}_{-0.029}$	$\mathcal{J}\,(10^{-6}, 10^{6})$	GP amplitude of the LCO-CTIO-A photometry
$\rho_{\mathrm{LCO\text{-}CTIO,\,B}}$	$977.2^{+1193.7}_{-959.5}$	$\mathcal{J}\,(10^{-6}, 10^{6})$	GP time-scale of the LCO-CTIO-B photometry
$\sigma_{\mathrm{LCO\text{-}CTIO,\,B}}$	$0.014^{+0.045}_{-0.011}$	$\mathcal{J}\,(10^{-6}, 10^{6})$	GP amplitude of the LCO-CTIO-B photometry
$\rho_{\mathrm{SPECULOOS\text{-}North}}$	$5.1^{+4.6}_{-3.9}$	$\mathcal{J}\,(10^{-6}, 10^{6})$	GP time-scale of the SPECULOOS-North photometry
$\sigma_{\mathrm{SPECULOOS\text{-}North}}$	$0.046^{+0.165}_{-0.035}$	$\mathcal{J}\,(10^{-6}, 10^{6})$	GP amplitude of the SPECULOOS-North photometry

APPENDIX C: POSTERIOR DISTRIBUTIONS OF KEY PARAMETERS IN THE FINAL JOINT FIT

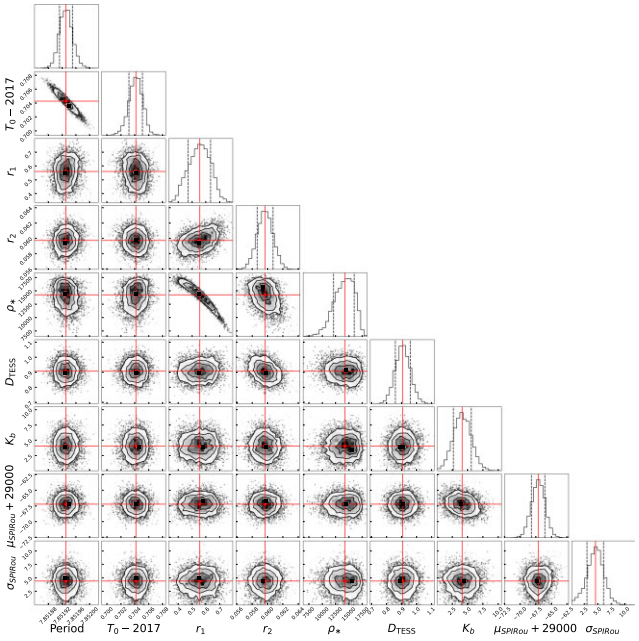

Figure C1. Posterior distributions of key parameters in the final joint fit (see Section 4.3). The red lines mark the median values of posterior distributions.

[1]*Department of Astronomy, Tsinghua University, Beijing 100084, China*
[2]*Oukaimeden Observatory, High Energy Physics and Astrophysics Laboratory, Cadi Ayyad University, Marrakech 644M+C9G, Morocco*
[3]*Departamento de Fisica e Astronomia, Faculdade de Ciencias, Universidade do Porto, Rua do Campo Alegre, 4169-007 Porto, Portugal*
[4]*Instituto de Astrofisica e Ciencias do Espaco, Universidade do Porto, CAUP, Rua das Estrelas, 4150-762 Porto, Portugal*
[5]*National Astronomical Observatories, Chinese Academy of Sciences, 20A Datun Road, Chaoyang District, Beijing 100012, China*
[6]*Département de Physique, IREX, Université de Montréal, Montréal, QC H3C 3J7, Canada*
[7]*Observatoire du Mont-Mégantic, Université de Montréal, Montréal, QC H3C 3J7, Canada*
[8]*Canada–France–Hawaii Telescope, 65-1238 Mamalahoa Hwy, Kamuela, HI 96743, USA*
[9]*Univ. de Toulouse, CNRS, IRAP, 14 Avenue Belin, F-31400 Toulouse, France*
[10]*Department of Astronomy, University of California Berkeley, Berkeley, CA 94720, USA*
[11]*Center for Astrophysics and Space Sciences, University of California, San Diego, 9500 Gilman Dr, La Jolla, CA 92093, USA*
[12]*Center for Astrophysics | Harvard & Smithsonian, 60 Garden Street, Cambridge, MA 02138, USA*
[13]*Department of Physics and Kavli Institute for Astrophysics and Space Research, Massachusetts Institute of Technology, Cambridge, MA 02139, USA*
[14]*Astrobiology Research Unit, Université de Liège, Allée du 6 Août 19C, B-4000 Liège, Belgium*
[15]*Department of Earth, Atmospheric and Planetary Science, Massachusetts Institute of Technology, 77 Massachusetts Avenue, Cambridge, MA 02139, USA*
[16]*Instituto de Astrofísica de Canarias (IAC), Calle Vía Láctea s/n, E-38200 La Laguna, Tenerife, Spain*
[17]*NASA Ames Research Center, Moffett Field, CA 94035, USA*
[18]*George Mason University, 4400 University Drive, Fairfax, VA 22030, USA*
[19]*Space Sciences, Technologies and Astrophysics Research (STAR) Institute, Universitd´e Liège, Allée du 6 Août 19C, B-4000 Liège, Belgium*
[20]*Center for Space and Habitability, University of Bern, Gesellschaftsstrasse 6, CH-3012 Bern, Switzerland*
[21]*School of Physics and Astronomy, University of Birmingham, Edgbaston, Birmingham B15 2TT, UK*
[22]*CEA, Université Paris-Saclay, Université de Paris, F-91191 Gif-sur-Yvette, France*
[23]*School of Aerospace Engineering, Tsinghua University, Beijing 100084, China*
[24]*NASA Exoplanet Science Institute, Caltech/IPAC, Mail Code 100-22, 1200 E. California Blvd., Pasadena, CA 91125, USA*
[25]*Instituto de Astronomía, Universidad Nacional Autónoma de México, Ciudad Universitaria, Ciudad de México 04510, México*
[26]*European Space Research and Technology Centre (ESTEC), European Space Agency (ESA), Keplerlaan 1, NL-2201 AZ Noordwijk, the Netherlands*
[27]*Centre for Astrophysics, University of Southern Queensland, West Street, Toowoomba, QLD 4350, Australia*
[28]*Department of Physics and Astronomy, Swarthmore College, Swarthmore, PA 19081, USA*
[29]*Department of Physics, Tsinghua University, Beijing 100084, China*
[30]*Department of Physics, University of Warwick, Coventry CV4 7AL, UK*
[31]*Cavendish Laboratory, JJ Thomson Avenue, Cambridge CB3 0HE, UK*
[32]*ETH Zurich, Department of Physics, Wolfgang-Pauli-Strasse 2, CH-8093 Zurich, Switzerland*
[33]*Department of Astronomy, University of Maryland, College Park, MD 20742, USA*
[34]*Patashnick Voorheesville Observatory, Voorheesville, NY 12186, USA*
[35]*Department of Aeronautics and Astronautics, Massachusetts Institute of Technology, 77 Massachusetts Avenue, Cambridge, MA 02139, USA*
[36]*Department of Astrophysical Sciences, Princeton University, 4 Ivy Lane, Princeton, NJ 08544, USA*

This paper has been typeset from a TEX/LATEX file prepared by the author.